ETH *zürich*

SITE CHARACTERIZATION REPORT
SWAS: Walenstadt (SG) - Sportplatz

Manuel Hobiger, Afifa Imtiaz, Donat Fäh

Last Modification: 17/10/2020

Contents

Summary

The free-field strong-motion station SWAS was built in Walenstadt (SG) next to the sports field. We performed a passive seismic array measurement to characterize the soil underneath the station.

The station is located on alluvial deposits above an old river bed. The fundamental peak at the station is around 0.47 Hz and corresponds to a 2-dimensional polarization. The Rayleigh wave ellipticity shows a second peak at 0.60 Hz, which we interpret as fundamental ellipticity peak corresponding to a singularity, where the Rayleigh wave particle motion changes its sense of rotation. The dispersion curves for Love and Rayleigh waves could be measured from around 0.55 to 7.5 Hz.

Joint inversions of Love and Rayleigh wave dispersion curves and the Rayleigh wave ellipticity angle give the preferred solutions for the site. The models show a gradual increase of the shear-wave velocity from around 128 to 151 m/s at the surface to less than 500 m/s at depths below 184 m, where the velocity increases strongly to over 800 m/s. This interface is identified as the seismic bedrock. The V_{S30} of the best models is about 227 m/s, corresponding to soil class C in EC8 and D in SIA261.

1 Introduction

In the framework of the second phase of the Swiss Strong Motion Network (SSMNet) renewal project, a new station was planned in Walenstadt (SG), on the eastern shore of the Walensee. The site selection resulted in the area around the sports field as the best site in the area. The new station, called SWAS, went operational on 21 March 2016. The location of the station is shown in Fig. 1.

Figure 1: Map showing the location of station SWAS in Walenstadt.

2 Geological setting

A geological map of the surroundings of station SWAS is shown in Fig. 2. The station is located on alluvial deposits of the Seez, as are all stations of the passive array measurement. The location of the station corresponds with the old river bed of the Seez.
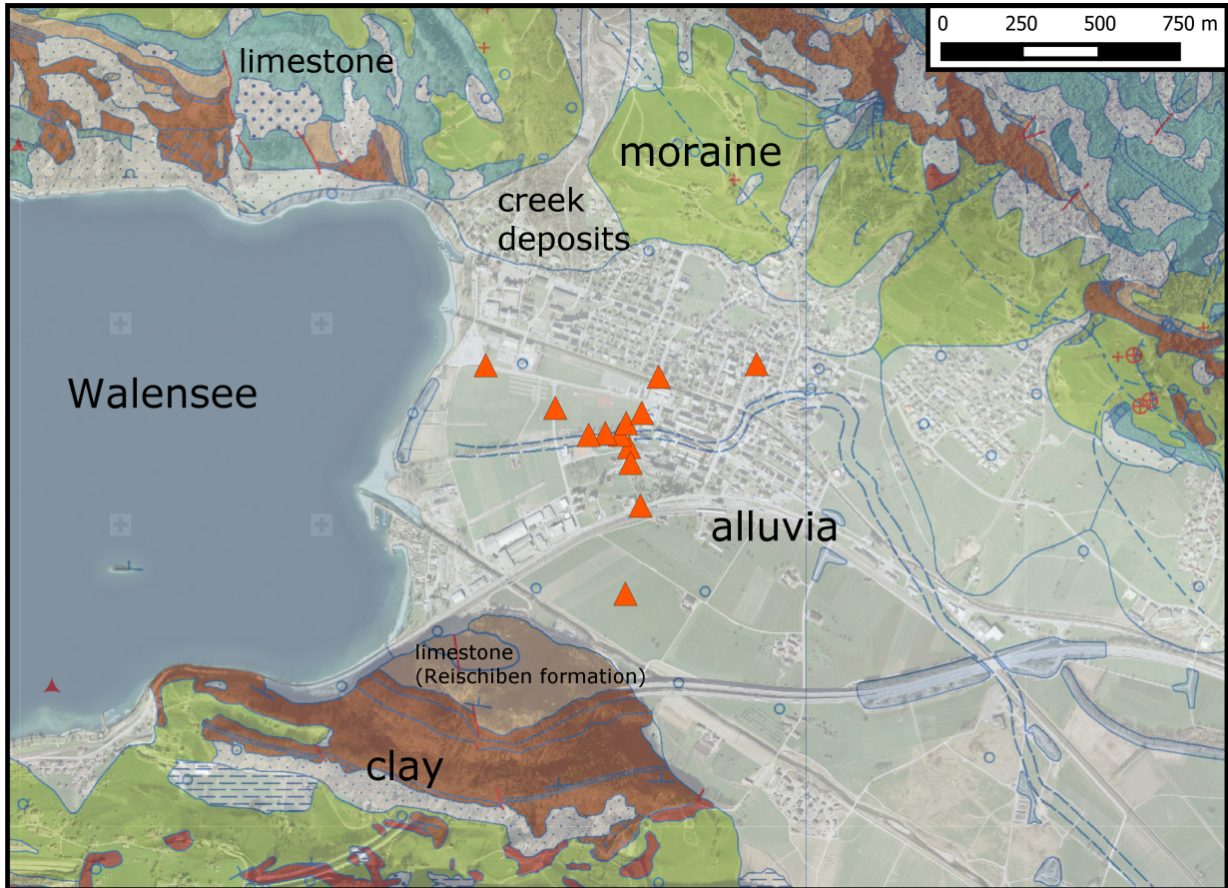

Figure 2: Geological map of the area around station SWAS with the locations of the stations of the passive seismic array (orange triangles). SWAS is located next to the central station of the array. According to the geological atlas, station SWAS and all array station lie on alluvial deposits. ©2020 swisstopo (JD100042)

3   Site characterization measurements

3.1   Data set

In order to characterize the local underground structure around station SWAS, a passive seismic array measurement was carried out on 15 October 2019. The layout of the seismic measurements is shown in Fig. 3.

The array consisted of 13 stations in total. It was planned to consist of four rings of three stations each around a central station, with ring radii of 42 m, 100 m, 225 m, and 500 m, respectively. SWAS45, the central station of the array, was located close to the permanent station SWAS. The final minimum and maximum inter-station distances in the array were 42.0 m and 862.4 m, respectively. The names of the array stations are composed of "SWAS" followed by a two-digit number (42 to 49, 52 to 55, 75). The seismic stations consisted of Lennartz 3C 5 s sensors connected to Centaur digitizers. A total of 12 digitizers were used, twelve sensors were connected to the A channels of the digitizers and another one to a B channel. The recording time of the array was 150 minutes.

The station locations have been measured by a differential GPS system (Leica Viva GS10) which was set up to measure with a precision better than 5 cm. This precision was achieved for all stations.

For the array analysis, the signals of the horizontal components have been reoriented by maximizing their cross-correlating with the signal of the central station in the frequency range between 0.1 and 0.3 Hz.
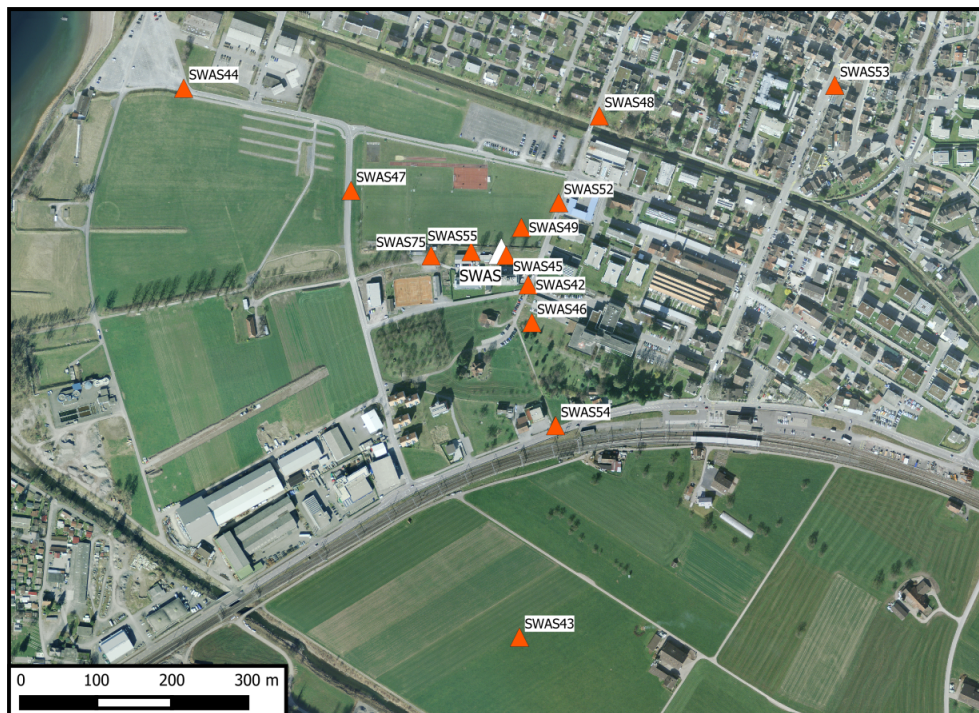

Figure 3: Layout of the array measurement around station SWAS. The location of SWAS is indicated by the white triangle, the locations of the stations for the passive seismic measurement by the orange triangles. ©2020 swisstopo (JD100042)

3.2 H/V curves

Fig. 4 shows the H/V curves determined with the time-frequency analysis method (Fäh et al., 2009) for all stations of the array. Most curves show a strong H/V peak at around 0.5 Hz and an amplitude of above 5, but some stations differ from this behavior. The map in Fig. 4 shows the peak frequencies at the respective stations. Major differences in the peak frqeuency are seen for the southern and the northeastern stations.
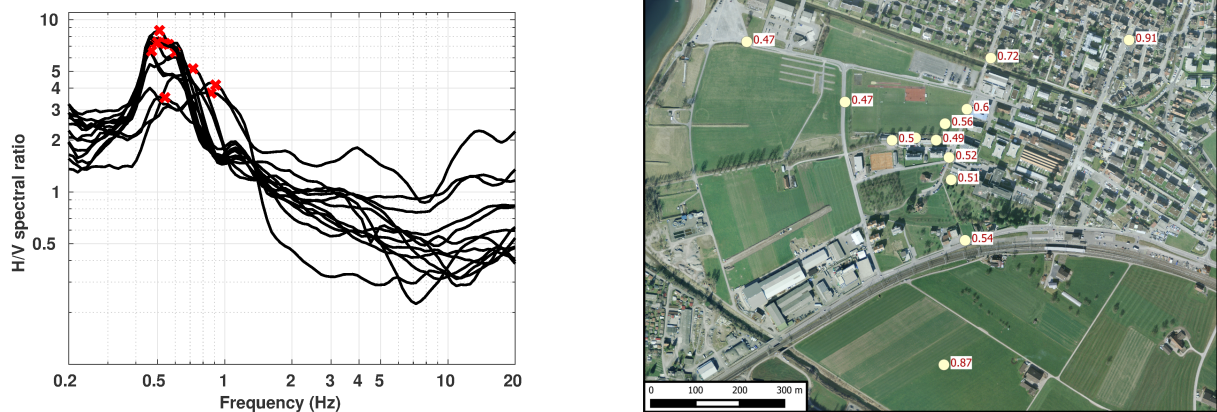

Figure 4: Left: Overview of the H/V measurements for the different stations of the array. Right: Map highlighting the H/V peak frequencies.

3.3 RayDec ellipticity curves

The RayDec technique (Hobiger et al., 2009) is supposed to eliminate the contributions of other wave types than Rayleigh waves and give a better estimate of the ellipticity than the classical H/V technique. The RayDec ellipticity curves for all stations of the array measurements are also shown in Fig. 5 and are mainly similar to the H/V curves. In red, stations with very similar ellipticity curves from the array center are shown (SWAS45, SWAS46, SWAS49, SWAS55, SWAS75). These stations consistently show a double peak with a first peak at 0.47 Hz and a second one at 0.6 Hz. Other three stations (SWAS42, SWAS47, SWAS52), shown in orange, exhibit a single peak at 0.6 Hz. The other stations, shown in grey, show less pronounced and more variable peaks.
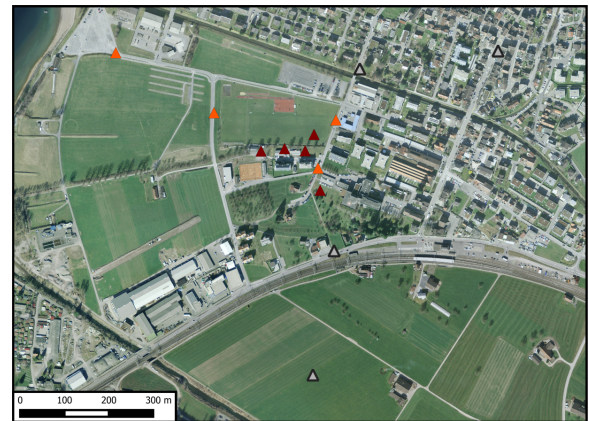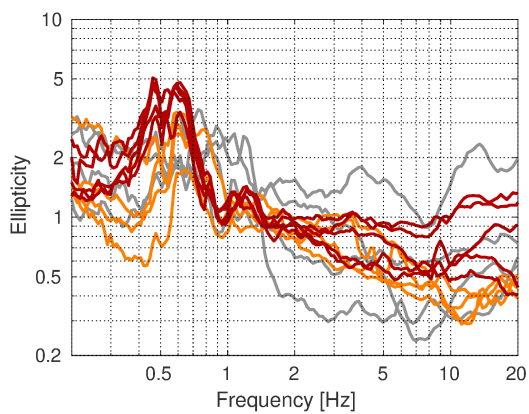

Figure 5: Left: RayDec ellipticities for all measurement stations, where the curves of three groups of stations are shown in red, orange and grey, respectively. Right: Overview map indicating the station attribution to the different groups.

3.4   Polarization analysis

The polarization analysis was performed according to Burjánek et al. (2010) and Burjánek et al. (2012). As the results for the different stations are different, all of them are shown in Figs 6 - 8. Many stations show a very pronounced linear polarization around 0.5 Hz, namely SWAS42, SWAS44, SWAS45, SWAS46, SWAS47, SWAS49, SWAS52, SWAS55, and SWAS75. These are exactly the red and orange stations from the RayDec analysis. We conclude that a 2-dimensional polarization effect is present in the valley, but mainly affecting the central part of the it. Stations to the south and the northeast do not show polarization effects.
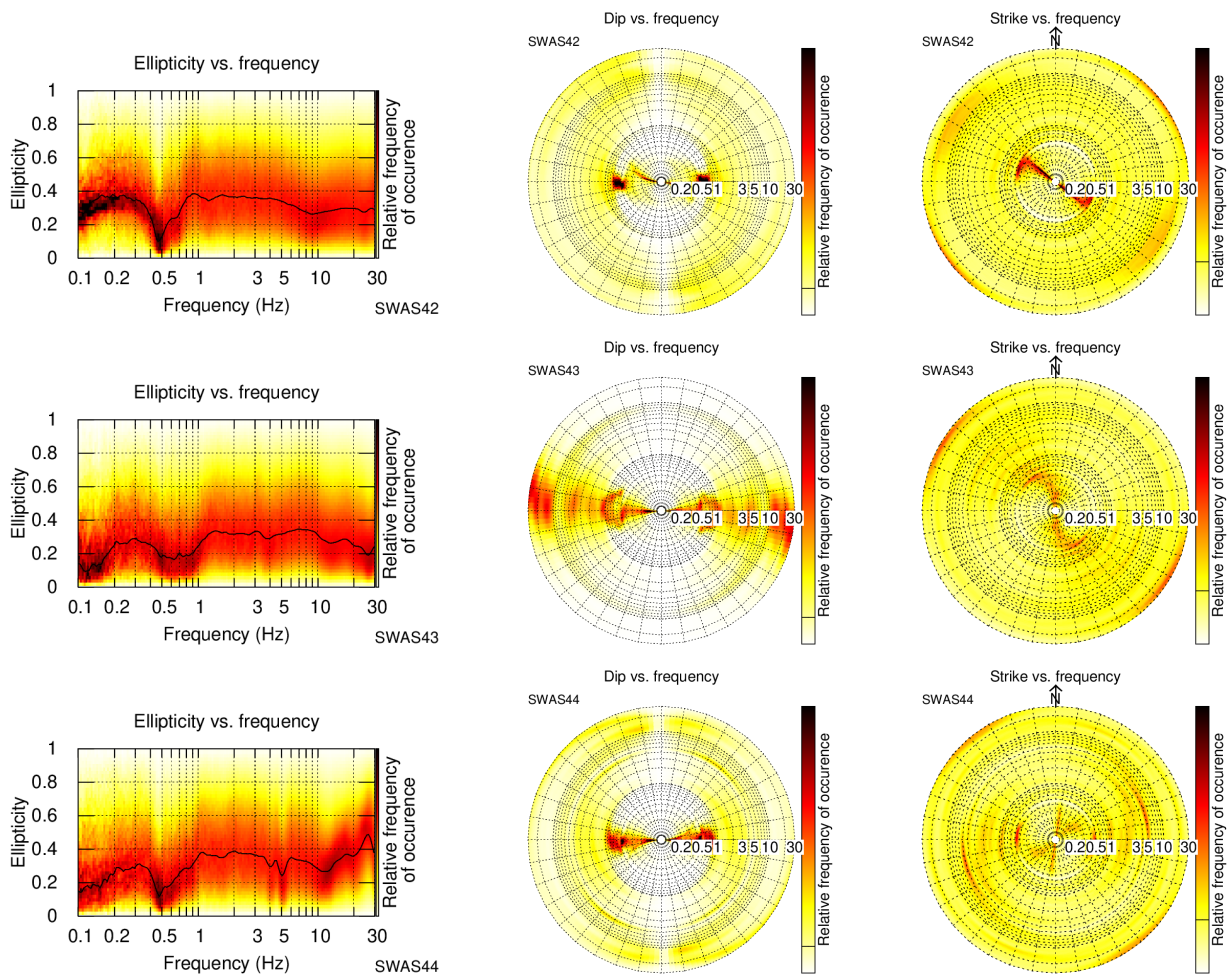

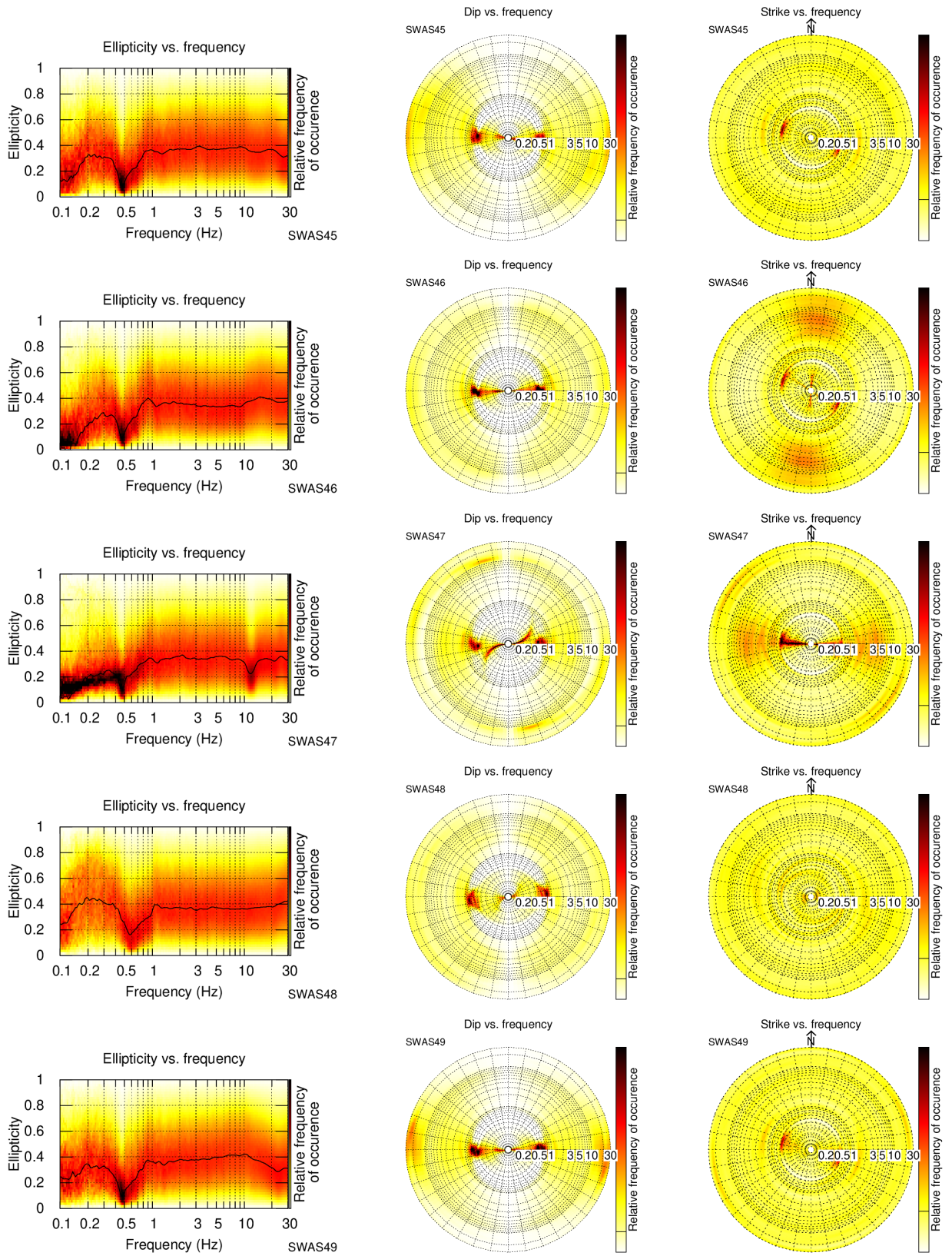Figure 6: Polarization analysis of stations SWAS42, SWAS43 and SWAS44.

Figure 7: Polarization analysis of stations SWAS45, SWAS46, SWAS47, SWAS48 and SWAS53.
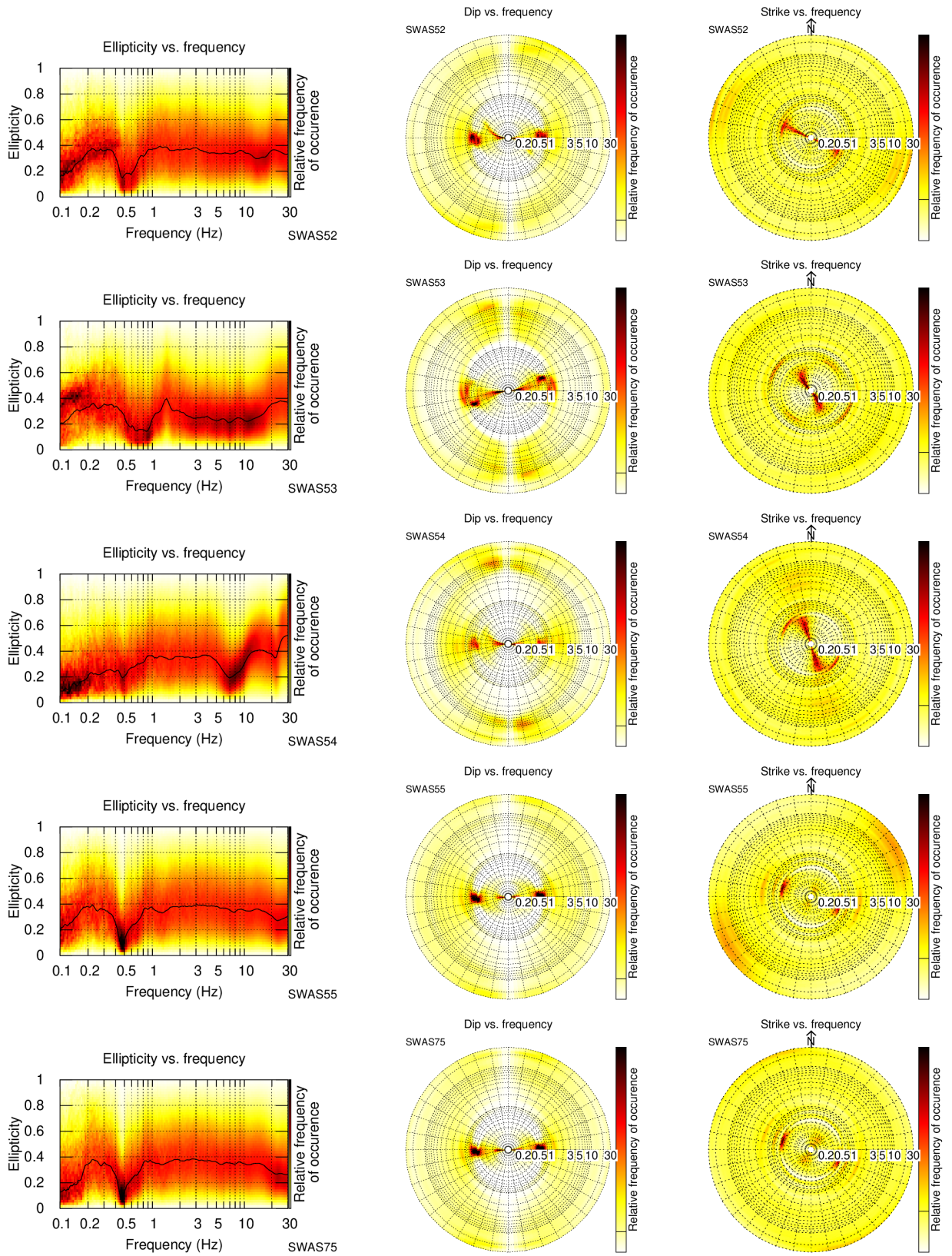
11

Figure 8: Polarization analysis of stations SWAS52, SWAS53, SWAS54, SWAS55 and SWAS75.

3.5 3-component high-resolution FK

The results of the 3-component high-resolution FK analysis (Poggi and Fäh, 2010) are shown in Fig. 9. On the transverse component, corresponding to Love waves, we can clearly identify a dispersion curve from 0.57 to 7.52 Hz, covering the accessible frequency range for the array.

On the vertical component, corresponding to Rayleigh waves, we can clearly identify one mode between 0.66 and 7.52 Hz, spanning the entire accessible frequency range. On the radial component, also related with Rayleigh waves, the results are less clear and we can only pick a dispersion curve between 0.90 and 2.00 Hz.

The corresponding ellipticity curve for the vertical component dispersion curve shows a steady decrease from around 1.5 below 1 Hz to 0.5 at 7 Hz. The curve for the radial component shows a peak between 1 and 1.5 Hz.

3.6 WaveDec

The results of the WaveDec (Maranò et al., 2012) processing are shown in Fig. 10. This technique estimates the properties of single or multiple waves simultaneously with a maximum likelihood approach. In order to improve the results, the parameter γ, which modifies the sharpness of the wave property estimation, has been tuned. Here, a value of $\gamma = 0.2$ was used, corresponding to a predominantly maximum likelihood estimation. The Love wave dispersion curve is clearly identified between 0.55 and 3.88 Hz.

The Rayleigh wave dispersion curve shows a lot of scatter and is retrieved between 0.62 and 1.86 Hz. At higher frequencies, no curve can be identified.

The ellipticity angle for the picked Rayleigh wave dispersion curve is clearly positive below 0.9 Hz, corresponding to prograde particle motion. Above that frequency, it might be either positive or negative, as both polarizations are present in the plot. As the fundamental Rayleigh wave mode is retrograde at low and high frequencies, we picked it as retrograde above 0.9 Hz. The absolute ellipticity value, obtained by taking the absolute value of the tangent of the ellipticity angle, shows a peak at around 0.65 Hz and decreases above. The trough, which should be visible around 0.9 Hz, is not clear.

As the performance of WaveDec at high frequencies is not satisfying, we tried to analyze only the inner parts of the array, i.e. the seven innermost array stations. However, it was not possible to reach higher frequencies with this smaller array and so these results are not shown.
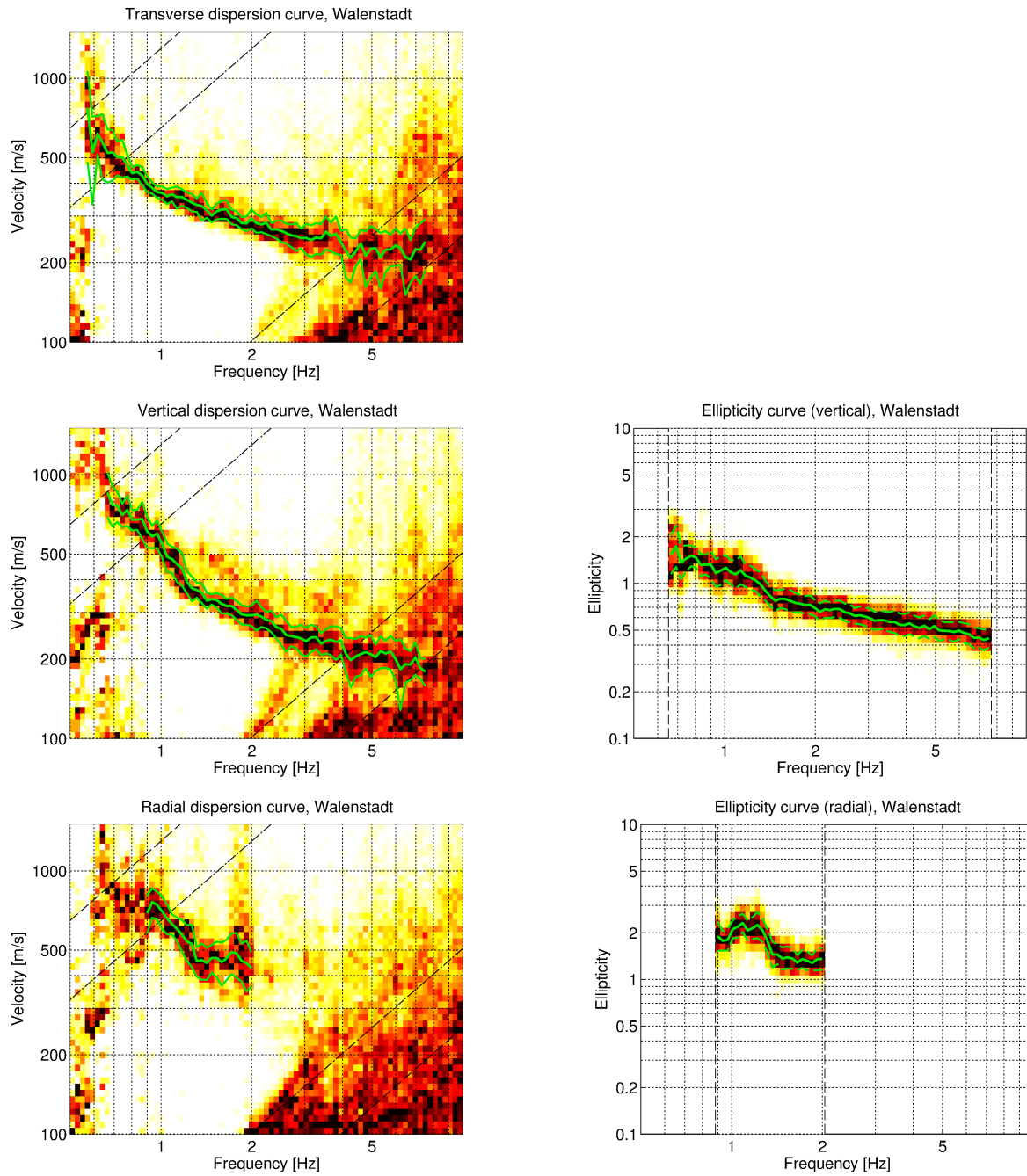
Figure 9: Dispersion and ellipticity curves obtained with the 3-component HRFK algorithm (Poggi and Fäh, 2010). In the left column, the dispersion curves for the transverse, vertical and radial components are shown, and in the right column the ellipticity curves corresponding to the dispersion curves picked on the vertical and radial components. The dashed and dotted black lines are the array resolution limits. The solid green lines are picked from the data, where the central line indicates the best values and the two outer lines the standard deviation.

14
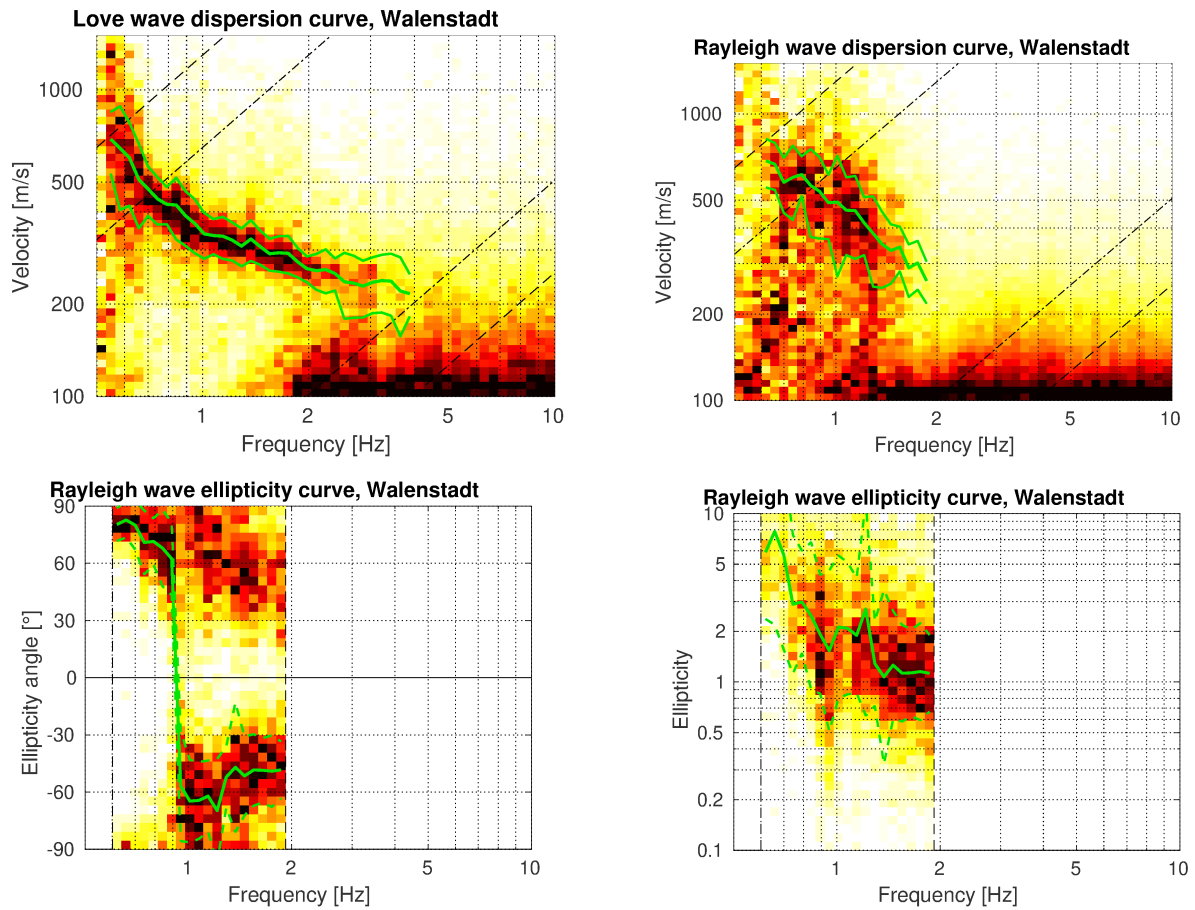
Figure 10: Top: Love (left) and Rayleigh (right) wave dispersion curves obtained with the WaveDec technique (Maranò et al., 2012). The dashed lines indicate the theoretical array resolution limits. Center: Rayleigh wave ellipticity angle curves for the two picked dispersion curves. Bottom: Rayleigh wave ellipticity curves, i.e. the absolute value of the tangent of the ellipticity angle curves shown above.

3.7 SPAC

Figure 11: SPAC curves for the array. The black data points contributed to the dispersion curve estimation.

The SPAC (Aki, 1957) curves of the vertical components have been calculated using the M-SPAC (Bettig et al., 2001) technique implemented in geopsy. Rings 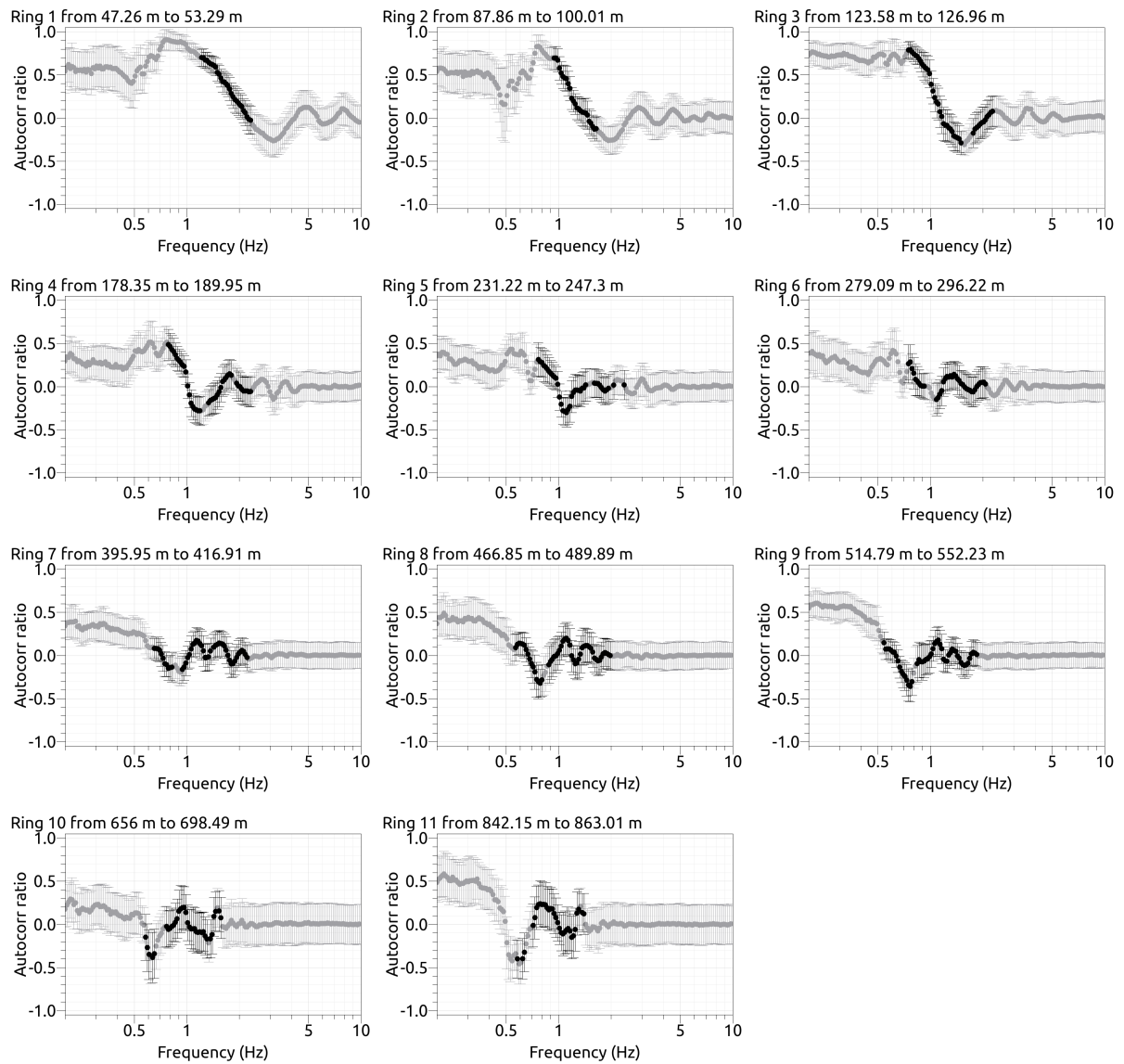with different radius ranges had been defined previously and for all station pairs with distance inside this radius range, the cross-correlation was calculated over a wide frequency range. These cross-correlation curves are averaged for all station pairs of the respective ring and give the SPAC curves. The rings are defined in such a way that at least three station pairs contribute and that their connecting vectors have a good directional coverage.

The SPAC curves for all defined rings are shown in Fig. 11. The black points indicate the data values which contributed to the final dispersion curve estimation, which was made with the function spac2disp of the geopsy package. The resulting dispersion curve is shown in Fig. 12.

The calculated SPAC curves have the shape of the theoretical Bessel functions. The retrieved Rayleigh wave dispersion curve ranges from 0.55 to 2.26 Hz.
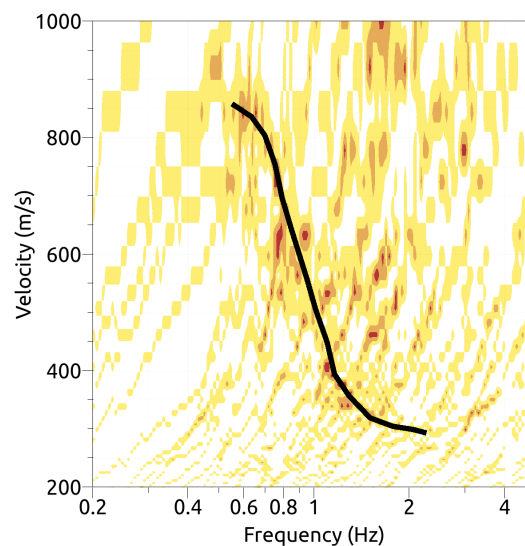

Figure 12: Resulting Rayleigh wave velocities. The black line corresponds to the picked dispersion curve.

3.8 Summary

Fig. 13 gives an overview of the dispersion and ellipticity curves determined by the different methods.

For Love waves, the HRFK and WaveDec results are in good overall agreement, with the HRFK curve reaching higher frequencies.

For Rayleigh waves, there is a also a good agreement between the different methods. The vertical HRFK curve is very similar to the SPAC curve, but reaches higher frequencies. The SPAC curve shows a flattening trend towards low frequencies, outside of the theoretical array resolution limits. The WaveDec curve is very close to the vertical HRFK and the SPAC curves above 1 Hz, but deviates slightly at lower frequencies.

The radial HRFK curve does not fit to the other curves and might correspond to a higher mode.

The ellipticity curves retrieved using the different methods are qualitatively similar. Two single-station ellipticity curves determined with RayDec are shown, the one for SWAS45, the array center, and the one for SWAS49, the closest station to the north. SWAS49 shows higher ellipticity values and a clearer double peak. This curve is actually in quite good agreement with the WaveDec curve, even if WaveDec shows even higher ellipticity values. The WaveDec curve coincides with the radial HRFK curve, even if their dispersion curves don't agree. Both show a small peak between 1 and 1.5 Hz, which is even visible in the RayDec curves.

The RayDec and HRFK curves were transformed to ellipticity angle by using the arctan function. As we cannot distinguish between prograde and retrograde particle motion with a single-station method, we account for both possibilities and the RayDec (and HRFK) curves are represented twice, once for each sense of rotation. In the ellipticity angle representation, the WaveDec curve shows prograde particle motion below 0.9 Hz and retrograde particle motion above, according to our interpretation during the picking. The interpretation of the ellipticity information is difficult because the observed 2-dimensional polarization effect also reflects in the ellipticity estimation. The double-peak in the RayDec curves makes the interpretation even more complex. The left peak, at around 0.47 Hz, is interpreted as a 2-D resonance effect. The right one, around 0.6 Hz, is not visible in the polarization analysis and can be interpreted as an ellipticity peak. As the particle motion above this peak is prograde, the peak must be a singularity if it belongs to the fundamental mode. Then, at lower frequencies, the particle motion has to be retrograde. Also at higher frequencies, the particle motion has to be retrograde, with an ellipticity trough in between, where the particle motion changes. This is the interpretation used for the picking of the WaveDec curve, where the trough frequency must be at around 0.9 Hz.
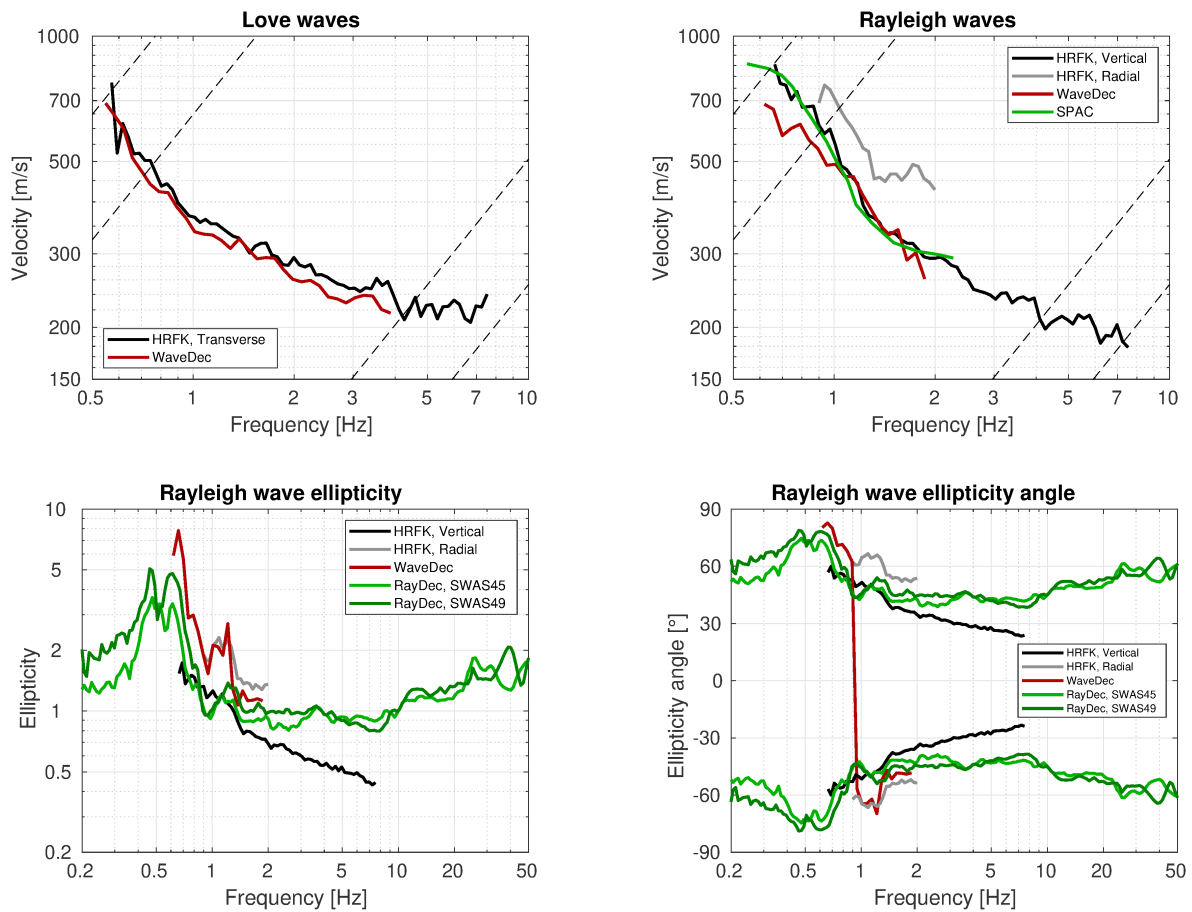
Figure 13: Overview of the Love and Rayleigh wave dispersion curves as well as the ellipticity and ellipticity angle curves for both arrays. The dashed lines indicate the theoretical resolution limits of array 1 (high frequencies) and array 1 (low frequencies). The RayDec ellipticity curve corresponds to station SWAS01.

4 Data inversion

4.1 Inversion parameterization

For the inversion, six different parameterizations have been used in total. The first five had free values of the depths and velocities of the different layers, ranging from four to eight layers (including half-space). The last parameterization had fixed layer depths and consisted of 21 layers in total. The P-wave velocities were allowed to vary up to $5000\,m/s$. The S-wave velocities were allowed to range from 50 to $3500\,m/s$. The deepest layers were parameterized to range to a depth of $600\,m$ maximum. The density was fixed to $2\,300\,kg/m^3$ for the lowest layer, to $1\,900\,kg/m^3$ for the superficial layer (or the first three layers in the fixed-layer case) and to $2\,100\,kg/m^3$ for all other layers. No low-velocity zones were allowed.

4.2 Inversion targets

We performed inversions with two different targets. The first consists of the Love and Rayleigh wave dispersion curves alone. The second target also includes the Rayleigh wave ellipticity angle. For the dispersion curves, the HRFK dispersion curves were used for both Love and Rayleigh waves, using the vertical component curve for Rayleigh waves.

The ellipticity angle curve obtained by WaveDec was used in target 2.

The details of the inversion targets are indicated in Table 1 and the corresponding curves are shown in Fig. 14.

Table 1: List of the different data curves used as target in the different inversions. For target 1, only the dispersion curves are used. For target 2, the dispersion and ellipticity angle curves are used.

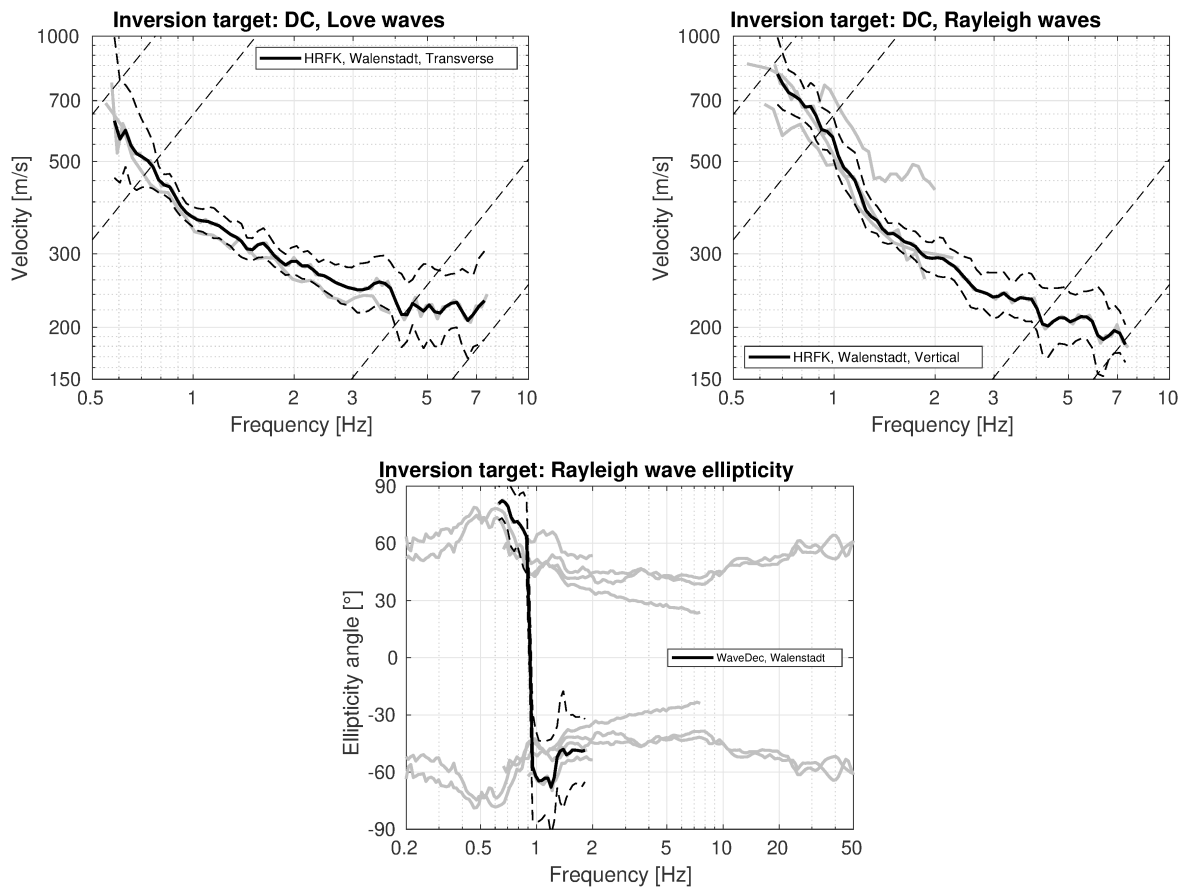| Method	Wave type	Mode	Curve type	Frequency range [Hz]
HRFK (T)	Love	fundamental	dispersion	0.58 - 7.39
HRFK (V)	Rayleigh	fundamental	dispersion	0.67 - 7.39
WaveDec	Rayleigh	fundamental	ellipticity angle	0.62 - 1.82

Figure 14: Overview of the dispersion (top) and ellipticity angle (bottom) curves used as targets for the different inversions.

4.3 Inversion results

We performed six inversions with different parameterizations for the different targets. For each parameterization, 20 different runs were performed, but only the one giving the best minimum misfit was kept. In Table 2, the obtained minimum misfit values for these inversions are given. Each inversion run with the four-layer parameterization produced around 100 000 total models. For the five- to seven-layer parameterizations, at least 150 000 models were generated per run in order to assure a good convergence of the solution, and for the eight-layer and fixed-depth inversions, at least 200 000 models were generated per run. The inversion names for inversions using target 1 (without ellipticity information) end by "1", the ones for target 2 (including ellipticity information) by "2". The results of the inversions are shown in Figs 15 - 26.

The different inversions with more than four layers yield similar misfit values and fit the data in a comparable way. The four-layer inversions give significantly larger minimum misfit values, indicating that this parameterization was inadequate to fit the data in a good way.

Table 2: List of inversions

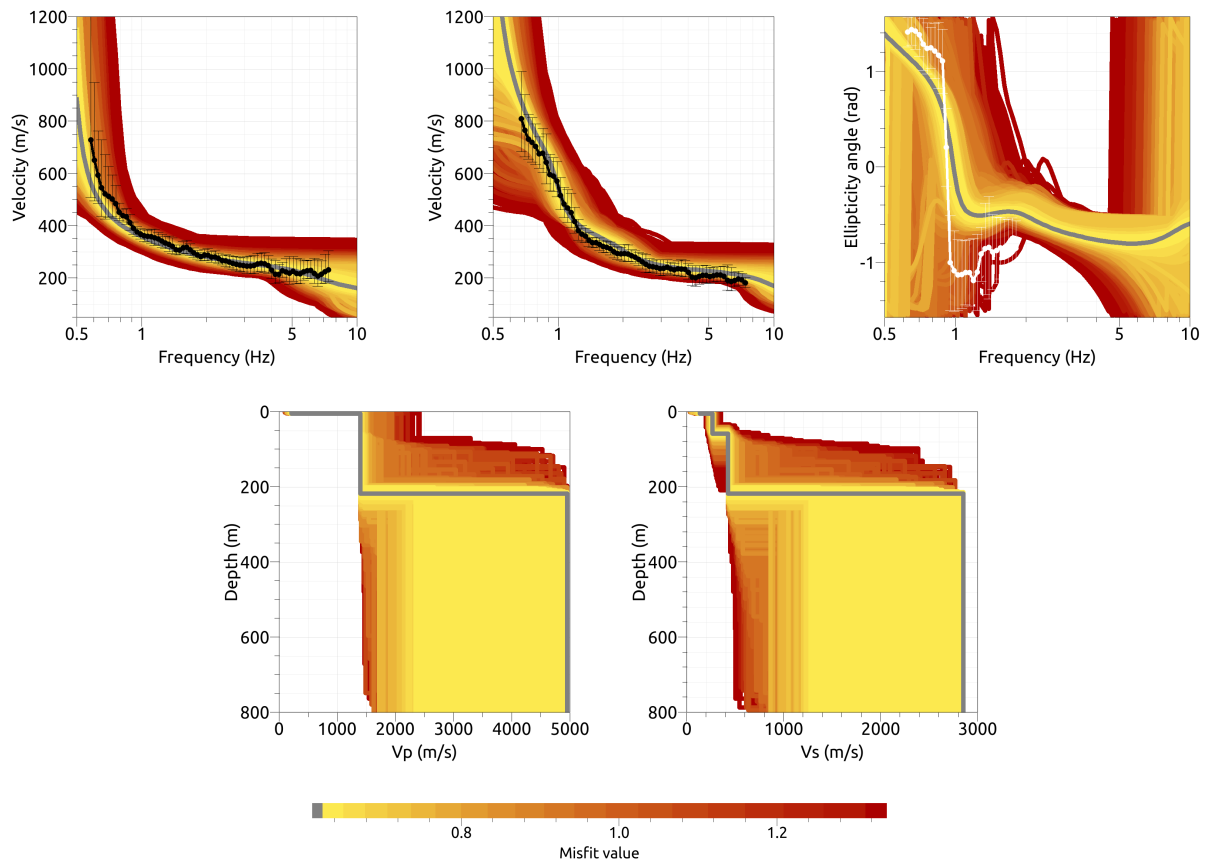| Inversion	Number of layers	Number of models	Minimum misfit
SWAS4l1	4	100 006	0.624
SWAS5l1	5	150 019	0.348
SWAS6l1	6	150 004	0.347
SWAS7l1	7	200 004	0.348
SWAS8l1	8	200 025	0.348
SWASfix1	21	200 004	0.344
SWAS4l2	4	100 013	0.941
SWAS5l2	5	150 036	0.563
SWAS6l2	6	150 008	0.591
SWAS7l2	7	200 003	0.591
SWAS8l2	8	200 013	0.591
SWASfix2	21	200 065	0.525

Figure 15: Inversion SWAS4l1. Top line: Dispersion curves for Love waves (left) and Rayleigh waves (center) and Rayleigh wave ellipticity angle (right) of the respective fundamental modes. Bottom line: P-wave velocity profiles (left), S-wave velocity profiles (center). All generated models are plotted on top of each other in the color corresponding to the respective misfit value. The black dots with error bars indicate the data points used for the inversion, the gray line indicates the best-fitting model. The white dots indicate ellipticity data not used for the inversion.
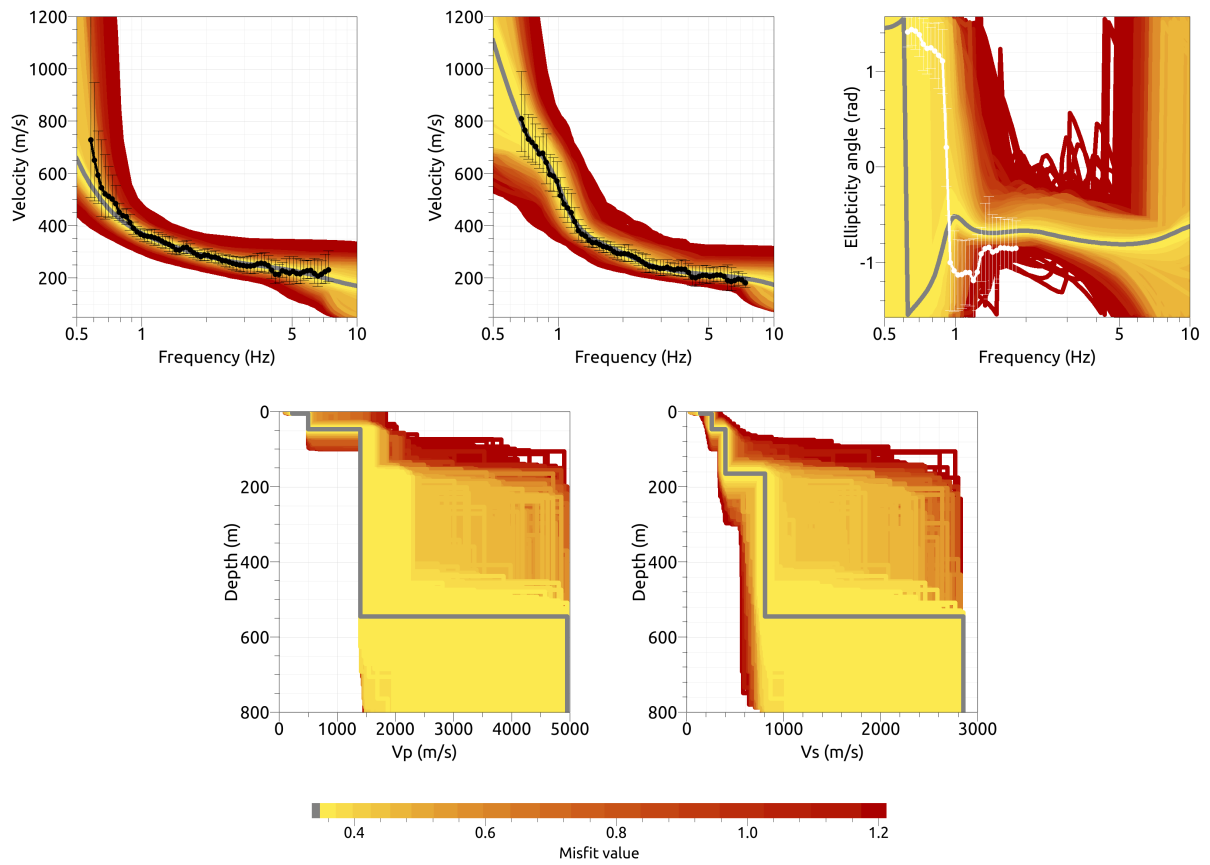
Figure 16: Inversion SWAS5l1. Top line: Dispersion curves for Love waves (left) and Rayleigh waves (center) and Rayleigh wave ellipticity angle (right) of the respective fundamental modes. Bottom line: P-wave velocity profiles (left), S-wave velocity profiles (center). All generated models are plotted on top of each other in the color corresponding to the respective misfit value. The black dots with error bars indicate the data points used for the inversion, the gray line indicates the best-fitting model. The white dots indicate ellipticity data not used for the inversion.
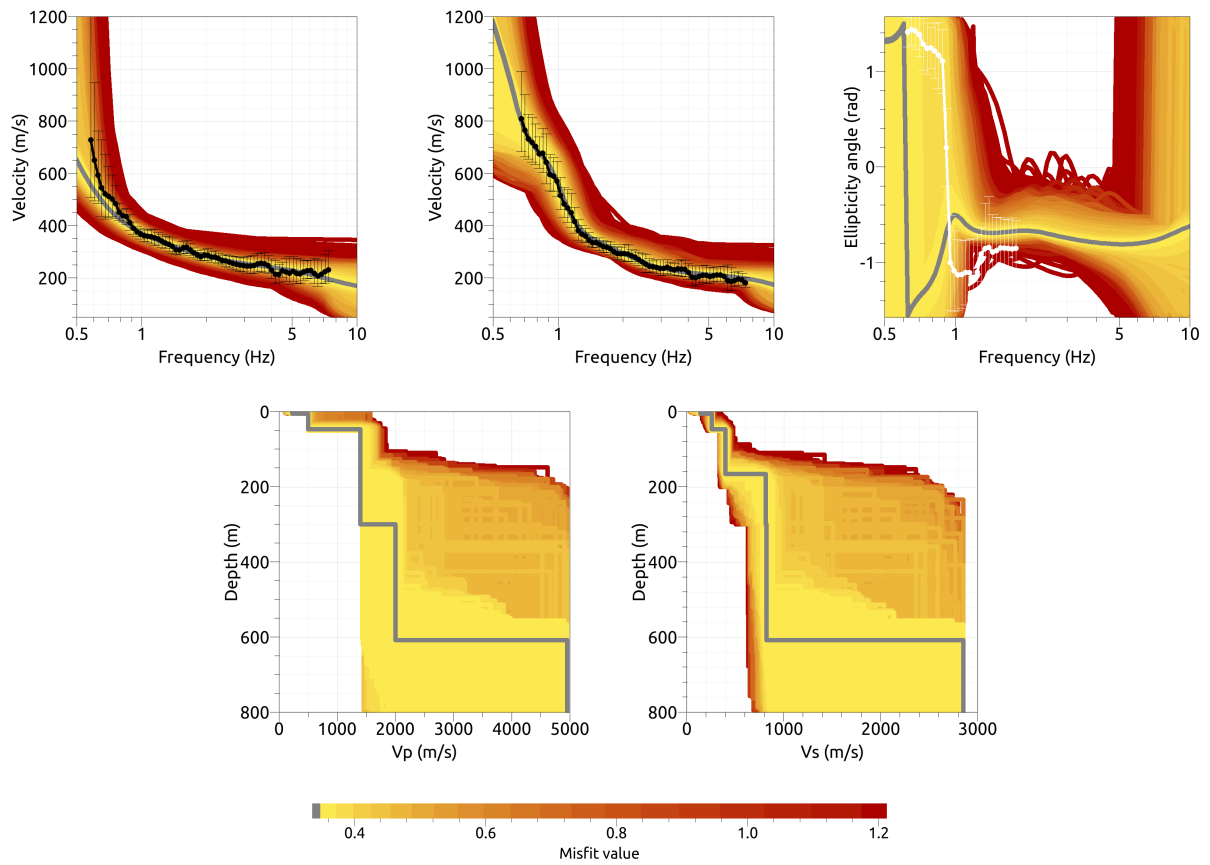
24

Figure 17: Inversion SWAS6l1. Top line: Dispersion curves for Love waves (left) and Rayleigh waves (center) and Rayleigh wave ellipticity angle (right) of the respective fundamental modes. Bottom line: P-wave velocity profiles (left), S-wave velocity profiles (center). All generated models are plotted on top of each other in the color corresponding to the respective misfit value. The black dots with error bars indicate the data points used for the inversion, the gray line indicates the best-fitting model. The white dots indicate ellipticity data not used for the inversion.
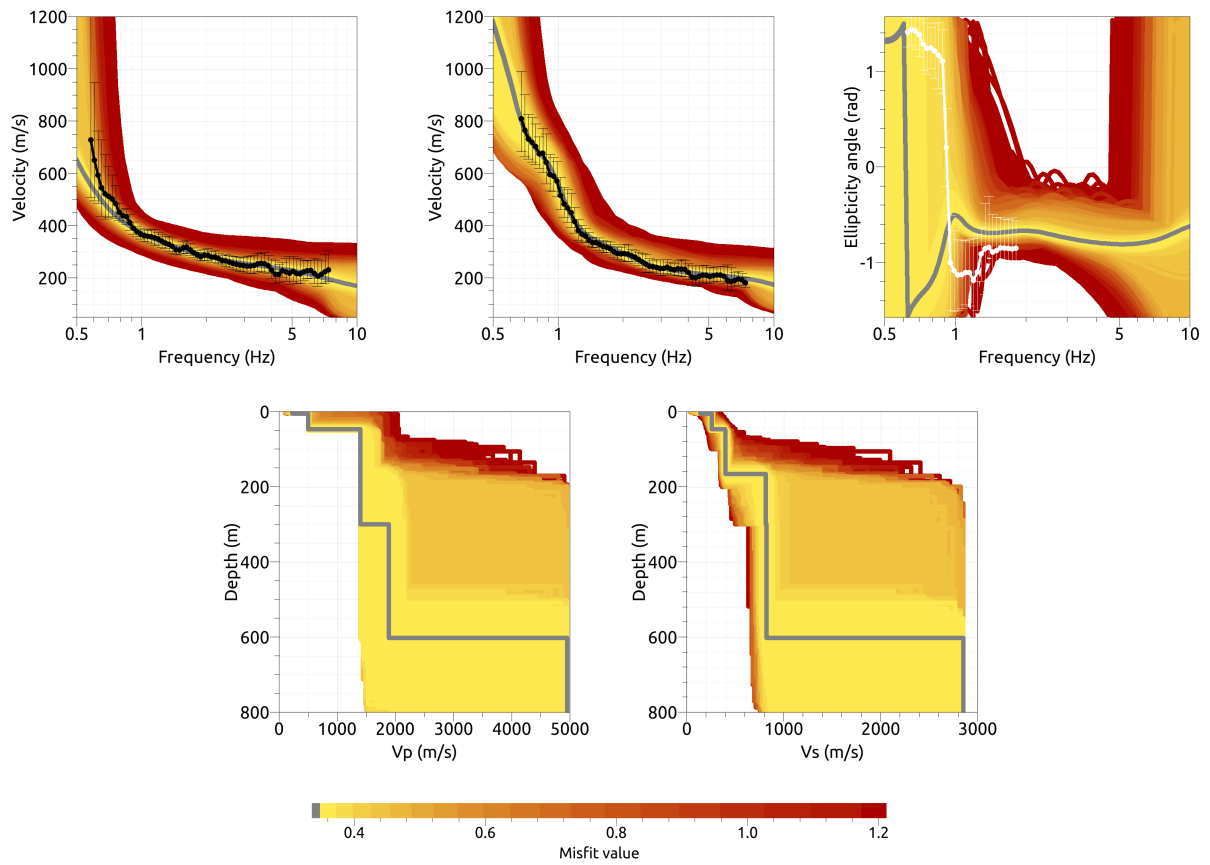
Figure 18: Inversion SWAS7l1. Top line: Dispersion curves for Love waves (left) and Rayleigh waves (center) and Rayleigh wave ellipticity angle (right) of the respective fundamental modes. Bottom line: P-wave velocity profiles (left), S-wave velocity profiles (center). All generated models are plotted on top of each other in the color corresponding to the respective misfit value. The black dots with error bars indicate the data points used for the inversion, the gray line indicates the best-fitting model. The white dots indicate ellipticity data not used for the inversion.
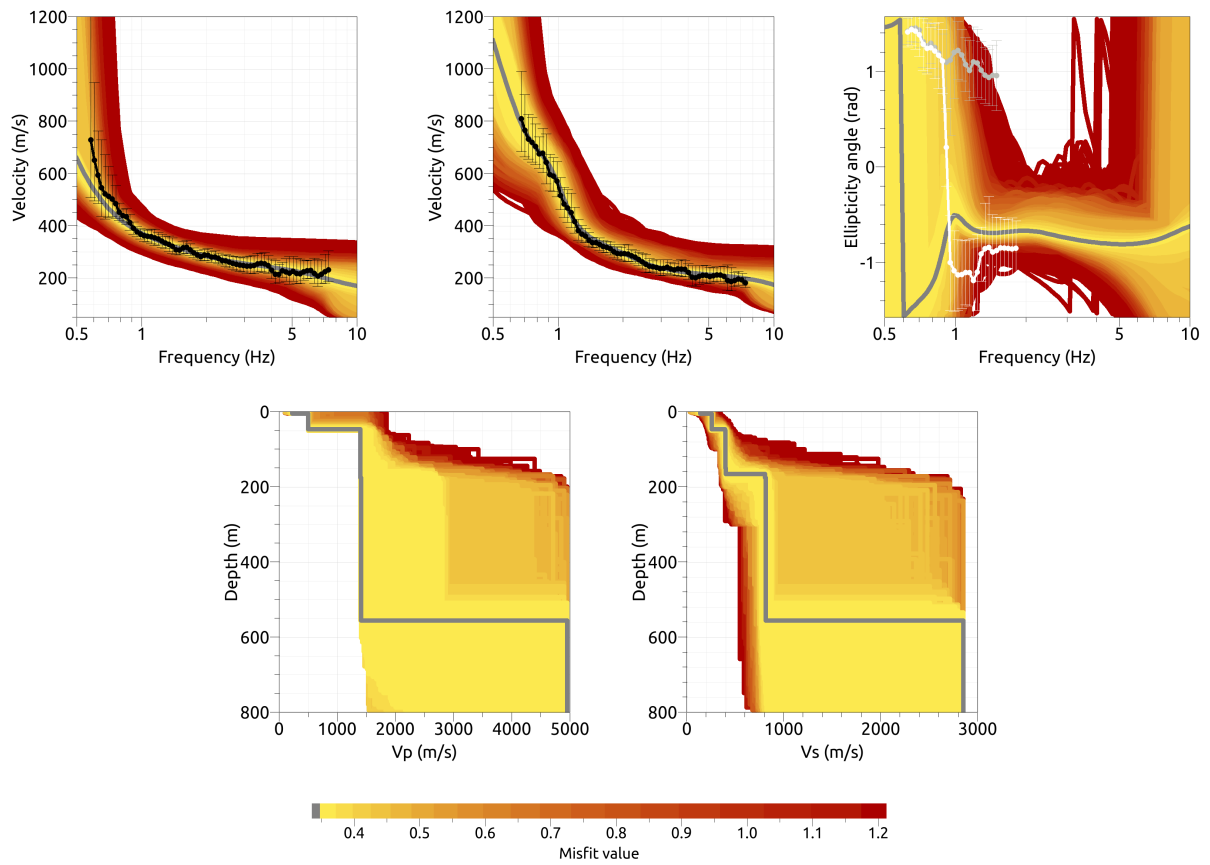
26

Figure 19: Inversion SWAS8l1. Top line: Dispersion curves for Love waves (left) and Rayleigh waves (center) and Rayleigh wave ellipticity angle (right) of the respective fundamental modes. Bottom line: P-wave velocity profiles (left), S-wave velocity profiles (center). All generated models are plotted on top of each other in the color corresponding to the respective misfit value. The black dots with error bars indicate the data points used for the inversion, the gray line indicates the best-fitting model. The white dots indicate ellipticity data not used for the inversion.
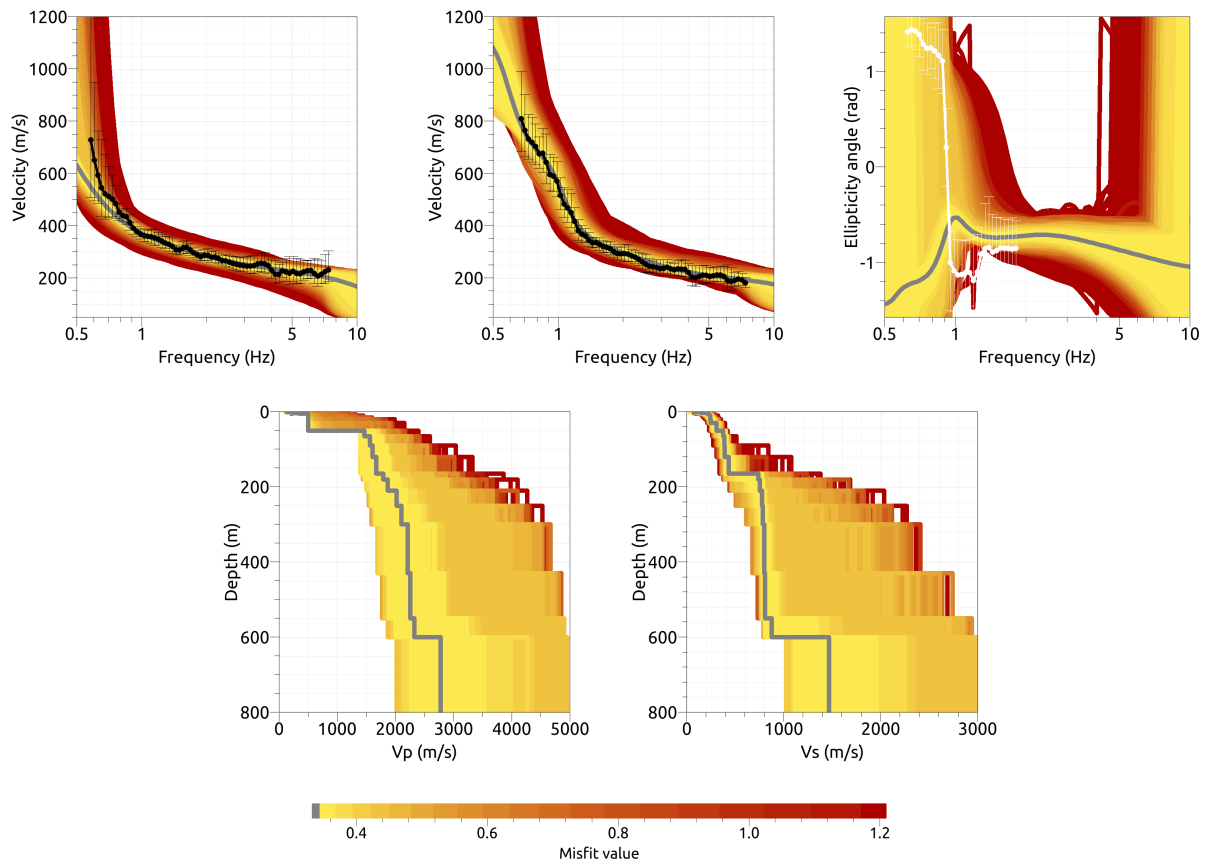
Figure 20: Inversion SWASfix1. Top line: Dispersion curves for Love waves (left) and Rayleigh waves (center) and Rayleigh wave ellipticity angle (right) of the respective fundamental modes. Bottom line: P-wave velocity profiles (left), S-wave velocity profiles (center). All generated models are plotted on top of each other in the color corresponding to the respective misfit value. The black dots with error bars indicate the data points used for the inversion, the gray line indicates the best-fitting model. The white dots indicate ellipticity data not used for the inversion.
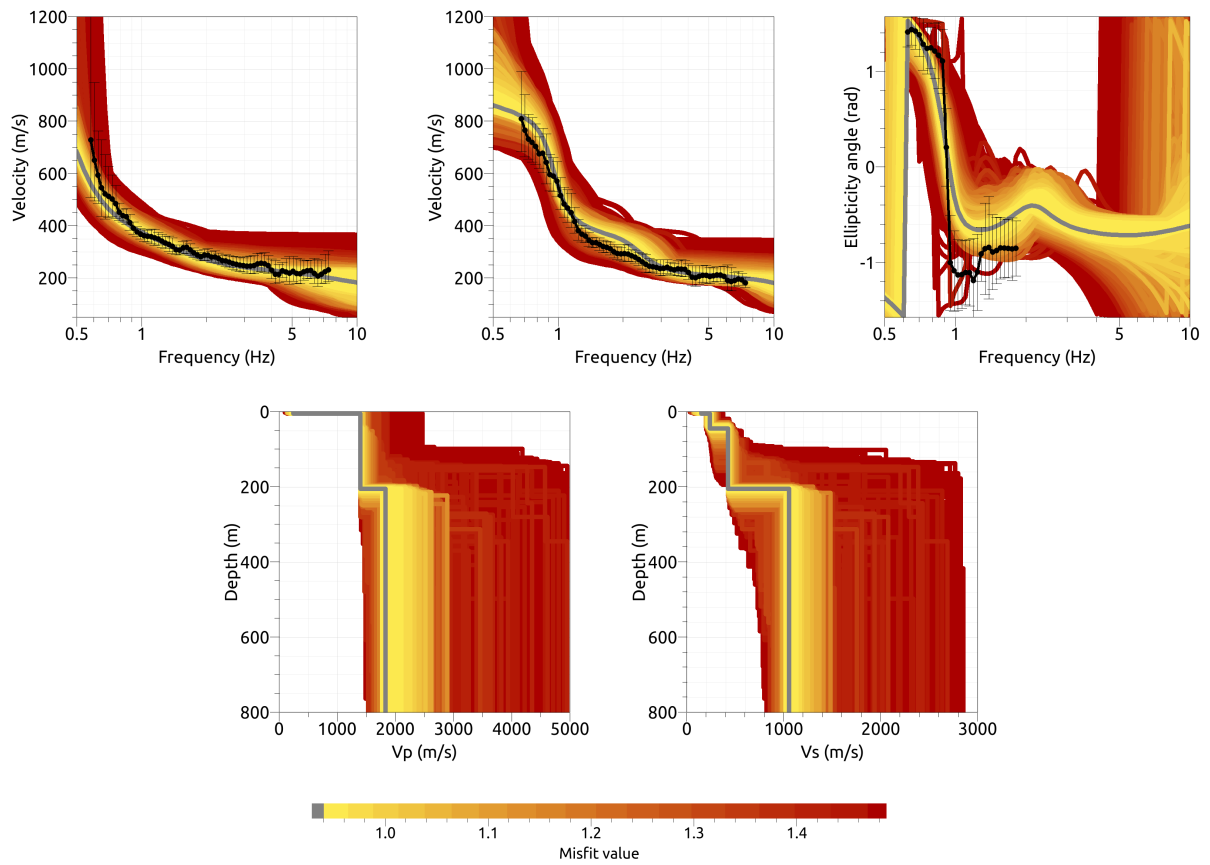
Figure 21: Inversion SWAS4l2. Top line: Dispersion curves for Love waves (left) and Rayleigh waves (center) and Rayleigh wave ellipticity angle (right) of the respective fundamental modes. Bottom line: P-wave velocity profiles (left), S-wave velocity profiles (center). All generated models are plotted on top of each other in the color corresponding to the respective misfit value. The black dots with error bars indicate the data points used for the inversion, the gray line indicates the best-fitting model. The white dots indicate ellipticity data not used for the inversion.

Figure 22: Inversion SWAS5l2. Top line: Dispersion curves for Love waves (left) and Rayleigh waves (center) and Rayleigh wave ellipticity angle (right) of the respective fundamental modes. Bottom line: P-wave velocity profiles (left), S-wave velocity profiles (center). All generated models are plotted on top of each other in the color corresponding to the respective misfit value. The black dots with error bars indicate the data points used for the inversion, the gray line indicates the best-fitting model. The white dots indicate ellipticity data not used for the inversion.
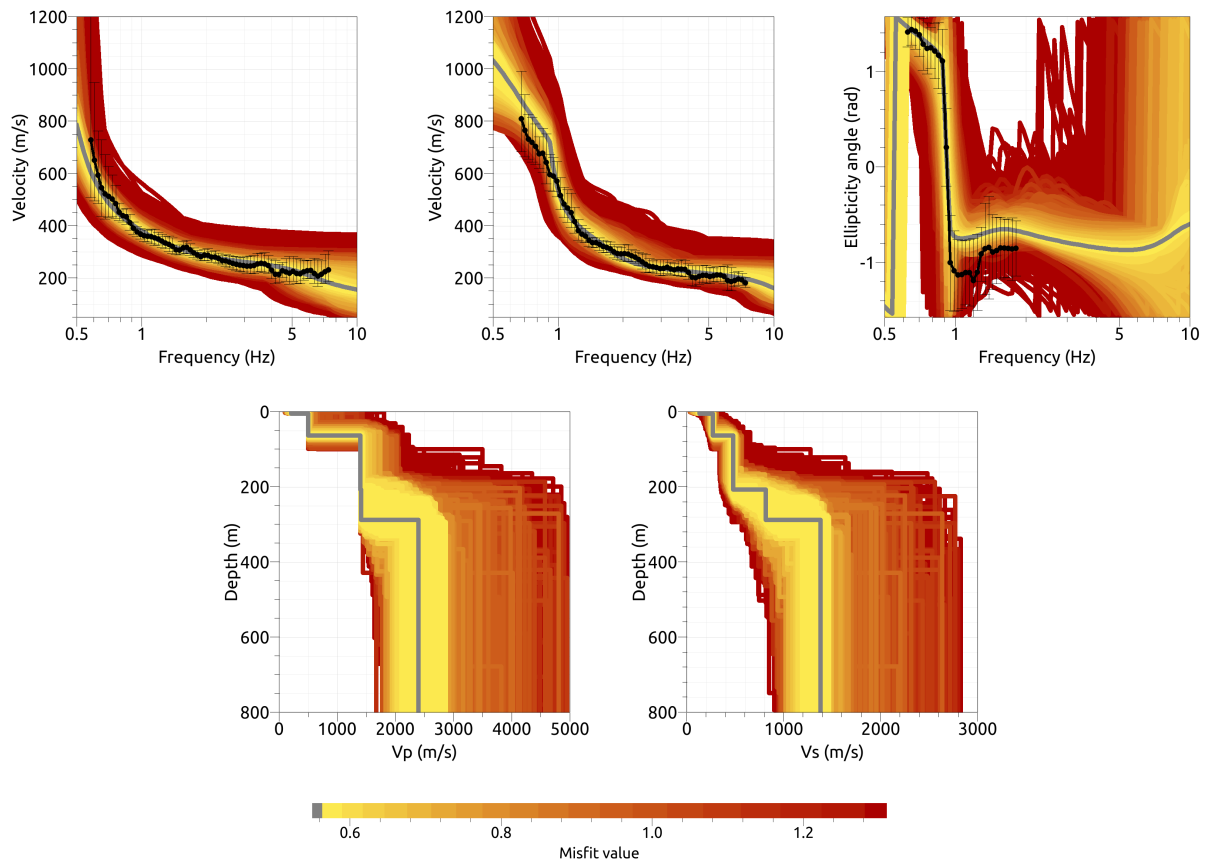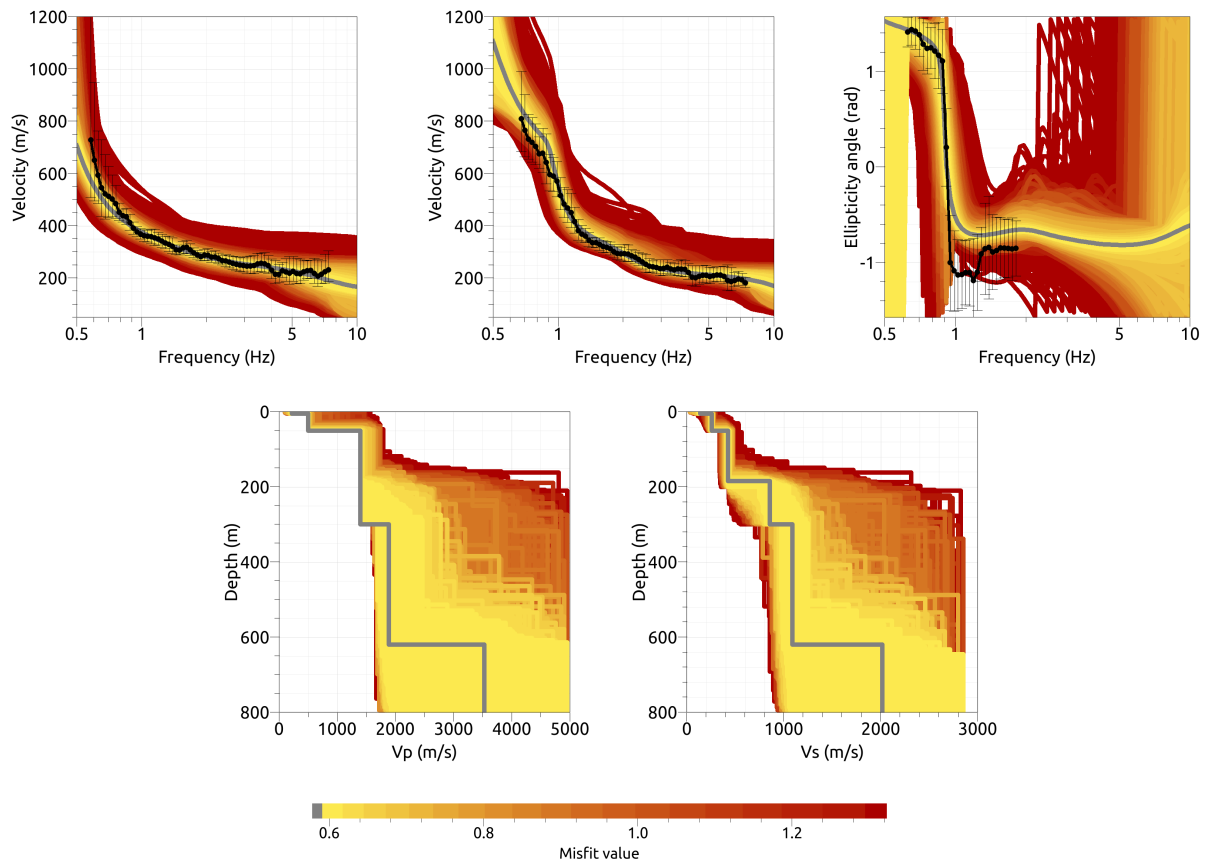
Figure 23: Inversion SWAS6l2. Top line: Dispersion curves for Love waves (left) and Rayleigh waves (center) and Rayleigh wave ellipticity angle (right) of the respective fundamental modes. Bottom line: P-wave velocity profiles (left), S-wave velocity profiles (center). All generated models are plotted on top of each other in the color corresponding to the respective misfit value. The black dots with error bars indicate the data points used for the inversion, the gray line indicates the best-fitting model. The white dots indicate ellipticity data not used for the inversion.

Figure 24: Inversion SWAS7l2. Top line: Dispersion curves for Love waves (left) and Rayleigh waves (center) and Rayleigh wave ellipticity angle (right) of the respective fundamental modes. Bottom line: P-wave velocity profiles (left), S-wave velocity profiles (center). All generated models are plotted on top of each other in the color corresponding to the respective misfit value. The black dots with error bars indicate the data points used for the inversion, the gray line indicates the best-fitting model. The white dots indicate ellipticity data not used for the inversion.
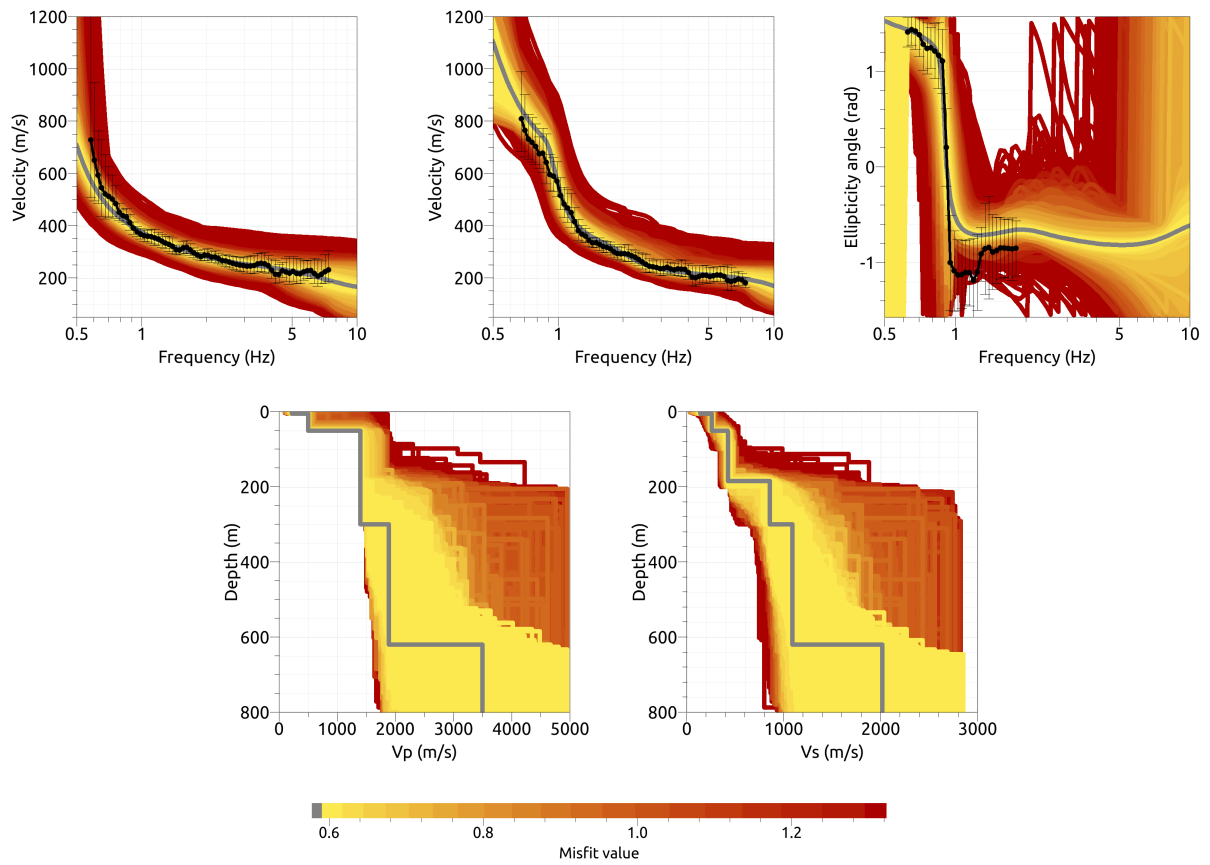
Figure 25: Inversion SWAS8l2. Top line: Dispersion curves for Love waves (left) and Rayleigh waves (center) and Rayleigh wave ellipticity angle (right) of the respective fundamental modes. Bottom line: P-wave velocity profiles (left), S-wave velocity profiles (center). All generated models are plotted on top of each other in the color corresponding to the respective misfit value. The black dots with error bars indicate the data points used for the inversion, the gray line indicates the best-fitting model. The white dots indicate ellipticity data not used for the inversion.
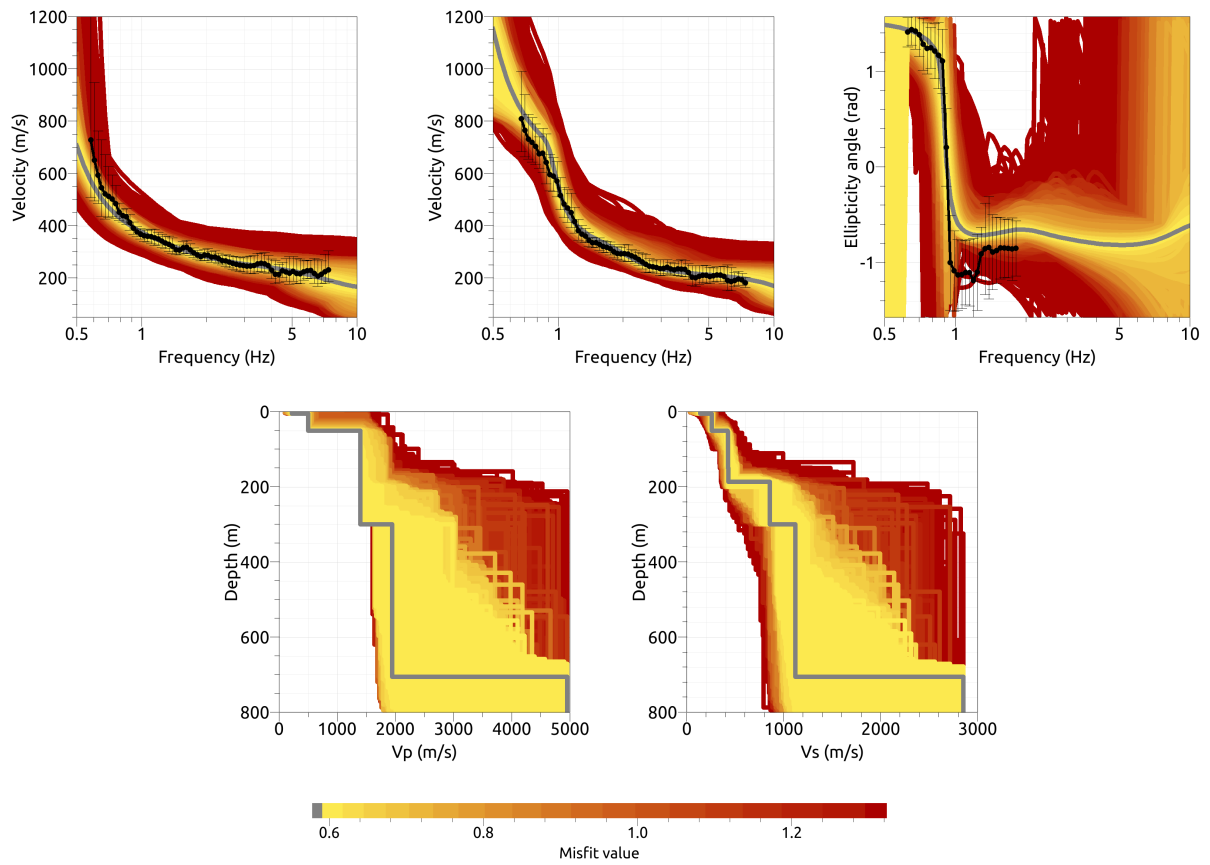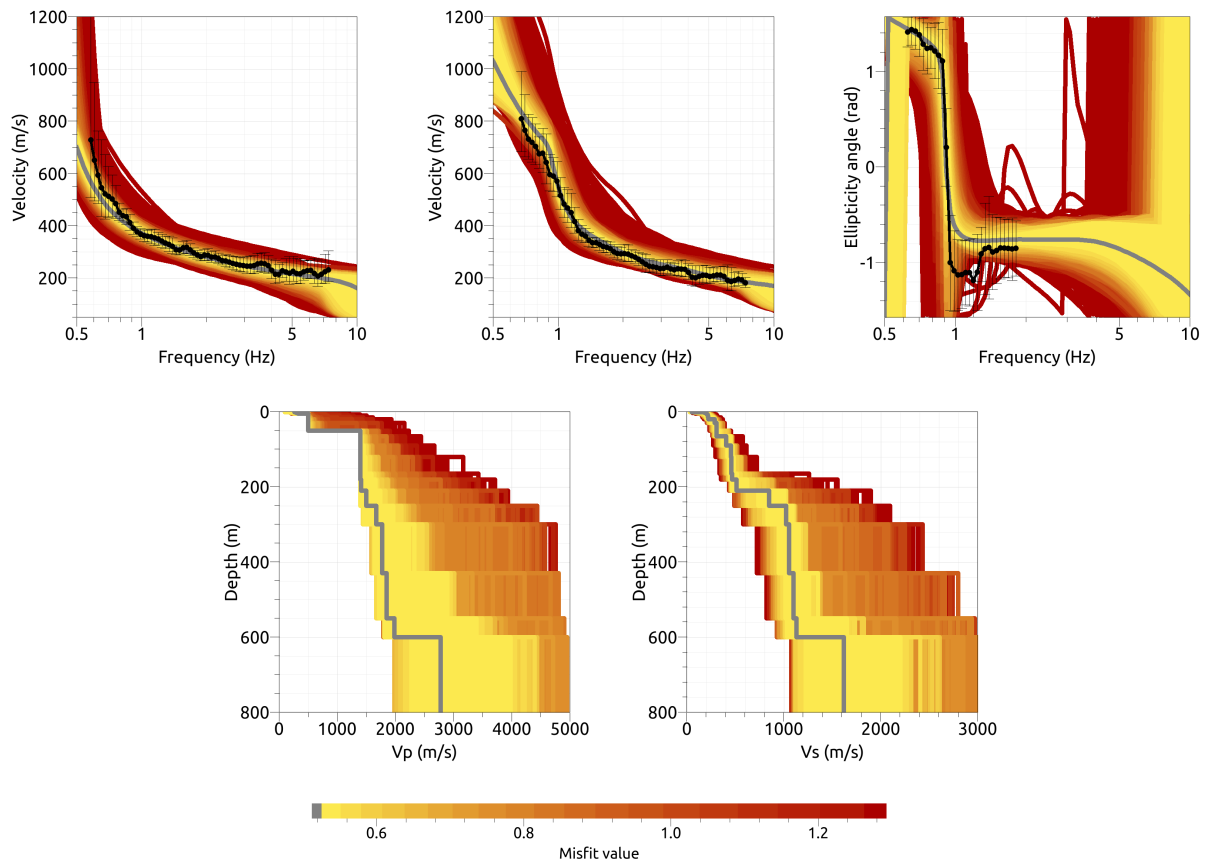
Figure 26: Inversion SWASfix2. Top line: Dispersion curves for Love waves (left) and Rayleigh waves (center) and Rayleigh wave ellipticity angle (right) of the respective fundamental modes. Bottom line: P-wave velocity profiles (left), S-wave velocity profiles (center). All generated models are plotted on top of each other in the color corresponding to the respective misfit value. The black dots with error bars indicate the data points used for the inversion, the gray line indicates the best-fitting model. The white dots indicate ellipticity data not used for the inversion.

4.4 Overview of the inversion result

The best-fitting models of all inversions are shown in Fig. 27. The four-layer inversions show significantly higher minimum misfit values and are discarded. As the highest inverted frequency was associated with a wavelength of about 25 m, we cannot expect to resolve the small-scale structure close to the surface. Therefore, the inversions with free layer depths place the first layer interface at 5 m, as this was the maximum thickness of the surface layer in the parameterization. All inversions for both targets find an S-wave velocity between 128 and 151 m/s for this layer. The models find a rather gradual increase and all models have shear-wave velocities below 500 m/s at over 150 m depth. The models resulting from target 1 are very similar. They show velocities of around 255 m/s down to about 47 m, where it increases to almost 400 m/s. At around 165 m depth, these models show an increase of the velocity to over 800 m/s, a value that the profiles keep down to over 500 m depth.

The models resulting from the inversions using target 2, i.e. forcing an ellipticity singularity below 0.6 Hz and a trough at around 0.9 Hz, show more variability. They find S-wave velocities of around 260 m/s down to depths between 50 and 64 m, where the velocity increases to velocities between 420 and 480 m/s. At depths between 184 and 210 m, the velocity increases to values between 814 and 855 m/s, followed by another increase to over 1000 m/s at depths between 288 and 300 m/s. These two velocity contrasts are strong enough to produce the singularity of the ellipticity at around 0.6 Hz. They are also in agreement with the value given by swisstopo for the thickness of the sedimentary layers, which range between 185 and 245 m in the center of the array.

The V_{S30} values for the inversions using target 1 range from 211.5 to 223.7 m/s (average value $221.2 \pm 5.4\,m/s$). For target 2, they range from 223.4 to 230.1 m/s (average value $226.6 \pm 3.4\,m/s$). This corresponds to soil class C in EC8 and D in SIA261.

In the inversions, we only used dispersion curves interpreted as fundamental modes. In Fig. 28, the Rayleigh wave dispersion curves for the fundamental and first higher modes for the best models resulting from the different inversions are compared with the measured dispersion curves of Fig. 13. The comparison shows that the dispersion curve picked on the radial component corresponds to the first higher mode, at least partly. Furthermore, the models for target 2 show an osculation point for the fundamental and first higher modes at around 0.8 Hz.
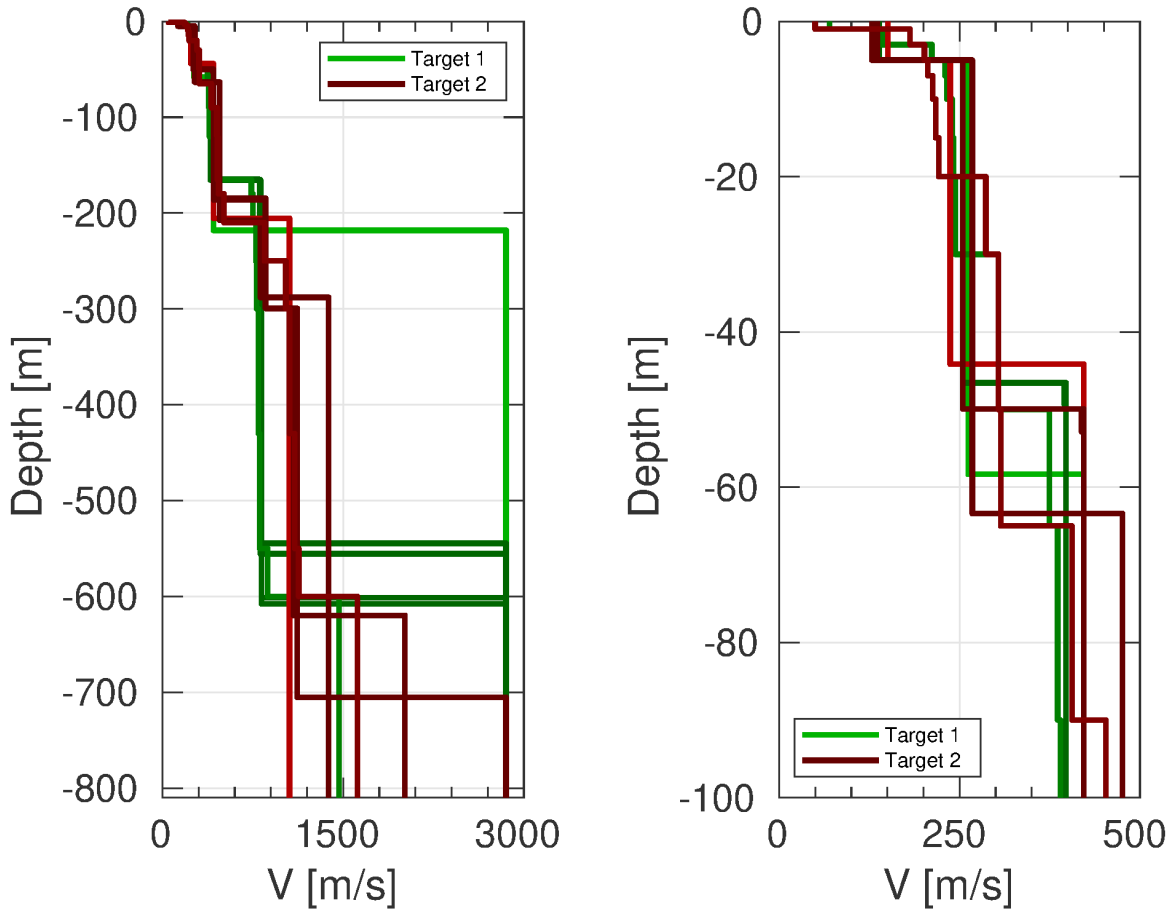
Figure 27: Overview of shear-wave velocity profiles of the best-fitting models of all inversions (left) and a zoom on the shallow part (right).
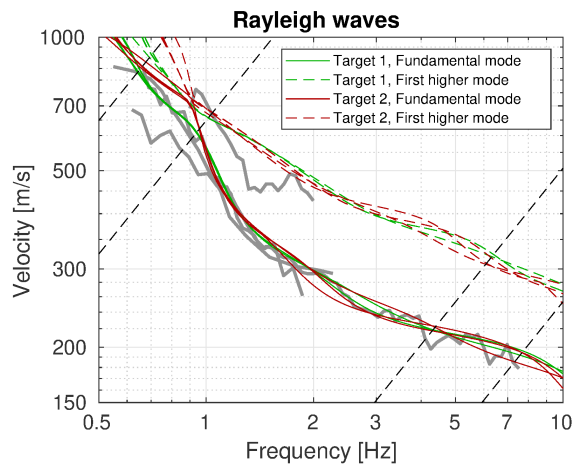

Figure 28: Comparison of the Rayleigh wave dispersion curves for the fundamental and first harmonic modes for the best models resulting from the inversion with the measured dispersion curves (as shown in Fig. 13).

4.5 Site amplification

In Figs 29 and 30, the theoretical amplification functions for the best models resulting from the five selected inversions for each target are compared with the empirical amplification. The empirical amplification for station SWAS is based on 24 events so far. The empirical amplification shows a strong peak around 0.5 Hz (no data below 0.5 Hz) and is quite flat with amplitudes around 4 up to high frequencies. The modelings for both targets cannot reproduce this result, but the one using target 2 shows a better agreement, especially around the fundamental peak, as it shows a single, wide peak there instead of two distinct peaks for target 1. The discrepancies between the 1D modeling and the empirical function are probably produced by the 2D polarization effects, which cannot be modeled with our 1D modeling. Edge-generated surface waves that impact the site and are not included in the modeling of vertically propagating S-waves might also play a role.
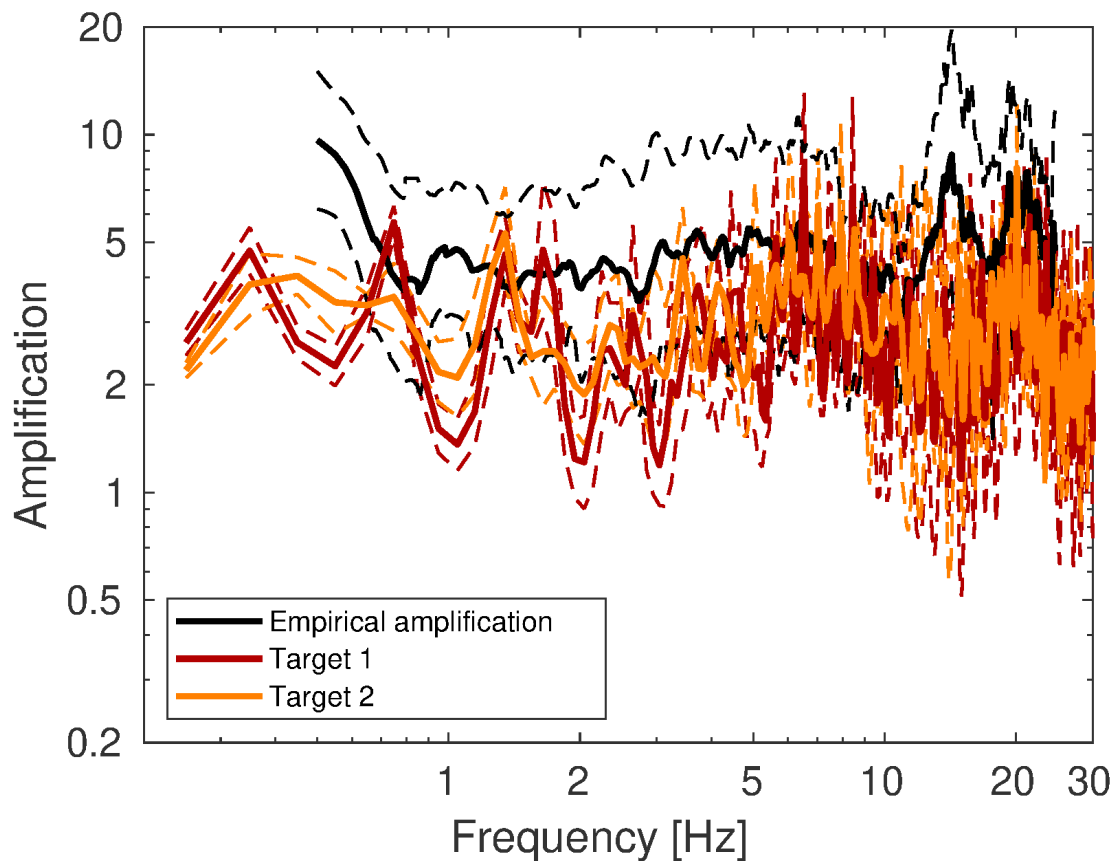

Figure 29: Comparison between the empirical amplification measured at station SWAS (black, with standard deviation), the modeled amplification for the best models using target 1 (red, with standard deviation) and target 2 (orange, with standard deviation).
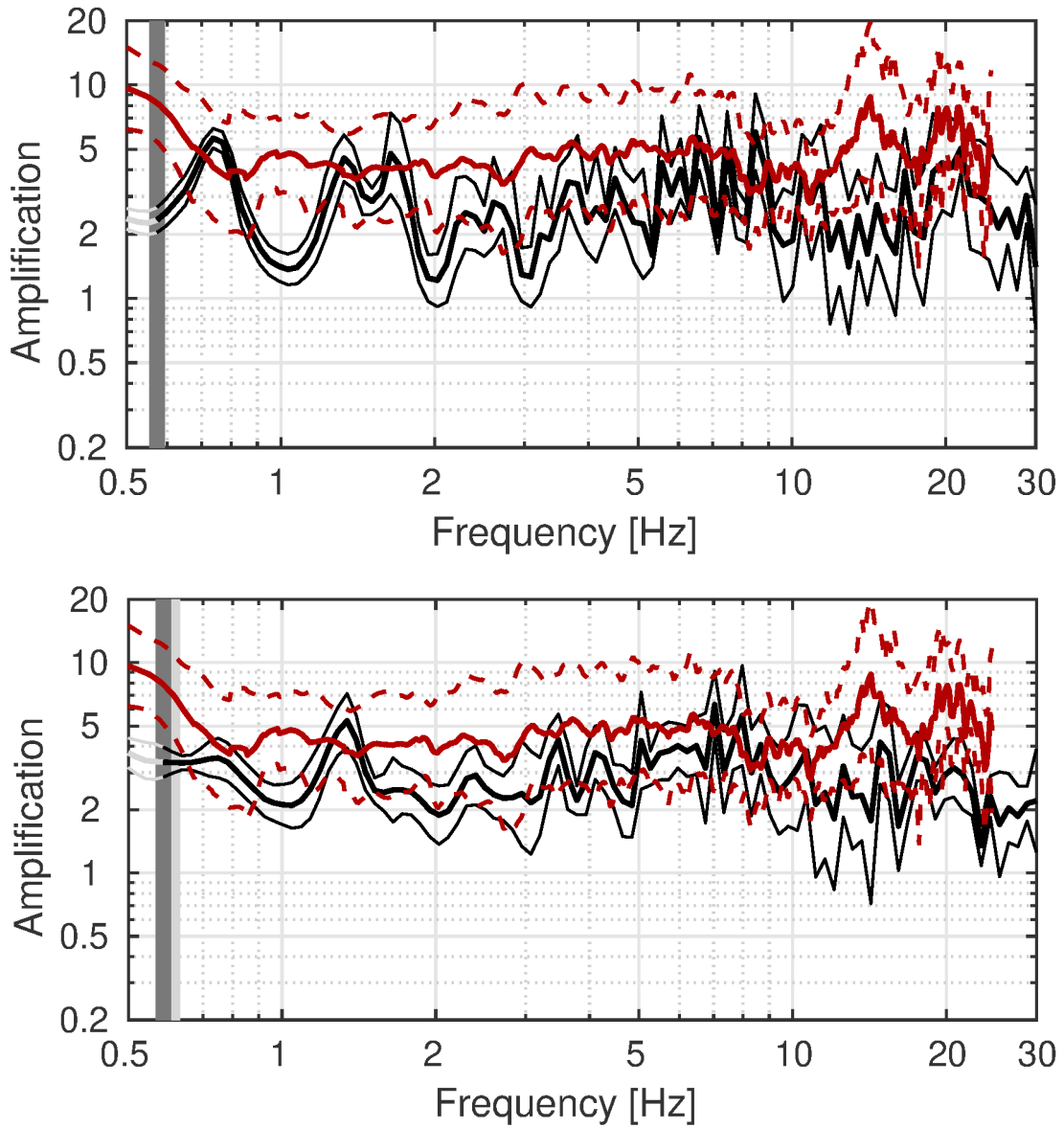
Figure 30: Comparison between the modeled amplification (in gray to black, with standard deviation) for the final set of best models of the different inversions using target 1 (top line) and target 2 (bottom line) and the empirical amplification measured at station SWAS (red, with standard deviation). The vertical light and dark grey bars correspond to the lowest frequency of the ellipticity and dispersion curves, respectively.

4.6 Quarter-wavelength representation

The quarter-wavelength velocity approach (Joyner et al., 1981) provides, for a given frequency, the average velocity at a depth corresponding to 1/4 of the wavelength of interest. It is useful to identify the frequency limits of the experimental data (the minimum frequency of the dispersion curve used in the inversion is 0.58 Hz, the minimum frequency used for the ellipticity inversion 0.62 Hz). The results using this proxy show that the dispersion curves constrain the profiles down to about 132 m using target 1 and 140 m using target 2 (Fig. 31). Moreover, the quarter wavelength impedance-contrast introduced by Poggi et al. (2012) is also displayed in the figure. It corresponds to the ratio between two quarter-wavelength average velocities, respectively from the top and the bottom part of the velocity profile, at a given frequency (Poggi et al., 2012). This curve shows a strong contrast at the fundamental frequency of the site.
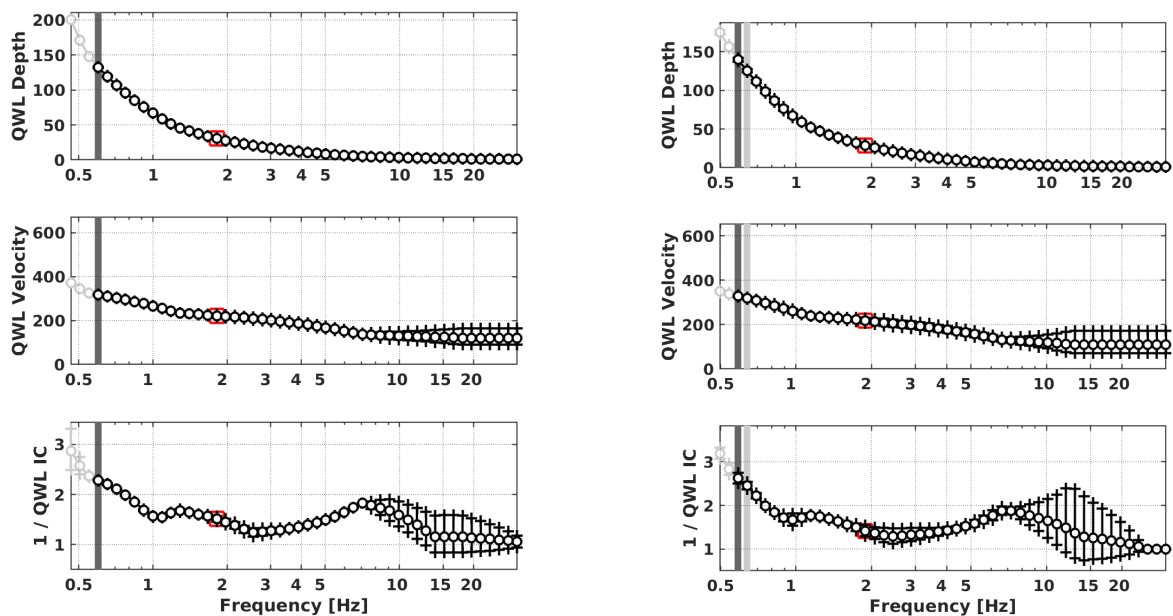

Figure 31: Quarter wavelength representation of the velocity profile for the best models of the inversions (left: target 1, right: target 2; top: depth, center: velocity, bottom: inverse of the impedance contrast). The black curves are constrained by the dispersion curves, the light grey curves are not constrained by the data. The red square corresponds to V_{S30}.

5 Conclusion

We performed a passive array measurement to characterize the soil underneath station SWAS in Walenstadt (SG), located on alluvial deposits, mainly above an old river bed. Because of the large size of the array (minimum and maximum inter-station distances of 42.0 and 862.4 m, respectively), the dispersion curves for Love and Rayleigh waves could be measured in a relatively low frequency range, from around 0.55 to 7.5 Hz for both wave types.

2-dimensional resonance effects are present, with a fundamental peak at around 0.47 Hz. The Rayleigh wave ellipticity shows a second peak at 0.60 Hz, which we interpret as fundamental ellipticity peak. According to the WaveDec results, this peak corresponds to a singularity, where the Rayleigh wave particle motion changes its sense of rotation. Joint inversions of Love and Rayleigh wave dispersion curves were performed, once without and once including the Rayleigh wave ellipticity angle information. The inversions including the ellipticity angle are in better agreement with the empirical amplification of the station and these models are therefore the preferred solution.

The models show a gradual increase of the shear-wave velocity from around 128 to 151 m/s at the surface to less than 500 m/s at depths below 184 m, where the velocity increases strongly to over 800 m/s. This is identified as the seismic bedrock.

The V_{S30} of the best models is about 227 m/s, corresponding to soil class C in EC8 and D in SIA261.

Acknowledgements

References

Aki, K. (1957). Space and time spectra of stationary stochastic waves, with special reference to microtremors. *Bull. Earthquake Res. Inst. Tokyo Univ.*, 35:415–456.

Bettig, B., Bard, P.-Y., Scherbaum, F., Riepl, J., Cotton, F., Cornou, C., and Hatzfeld, D. (2001). Analysis of dense array noise measurements using the modified spatial auto-correlation method (SPAC): application to the Grenoble area. *Boll. Geof. Teor. Appl.*, 42:281–304.

Burjánek, J., Gassner-Stamm, G., Poggi, V., Moore, J. R., and Fäh, D. (2010). Ambient vibration analysis of an unstable mountain slope. *Geophys. J. Int.*, 180:820–828.

Burjánek, J., Moore, J. R., Molina, F. X. Y., and Fäh, D. (2012). Instrumental evidence of normal mode rock slope vibration. *Geophys. J. Int.*, 188:559–569.

Fäh, D., Wathelet, M., Kristekova, M., Havenith, H., Endrun, B., Stamm, G., Poggi, V., Burjanek, J., and Cornou, C. (2009). Using ellipticity information for site characterisation. NERIES deliverable JRA4 D4, available at http://www.neries-eu.org.

Hobiger, M., Bard, P.-Y., Cornou, C., and Le Bihan, N. (2009). Single station determination of Rayleigh wave ellipticity by using the random decrement technique (RayDec). *Geophys. Res. Lett.*, 36.

Joyner, W. B., Warrick, R. E., and Fumal, T. E. (1981). The effect of Quaternary alluvium on strong ground motion in the Coyote Lake, California, earthquake of 1979. *Bull. Seismol. Soc. Am.*, 71(4):1333–1349.

Maranò, S., Reller, C., Loeliger, H.-A., and Fäh, D. (2012). Seismic waves estimation and wavefield decomposition: Application to ambient vibrations. *Geophys. J. Int.*, 191:175–188.

Poggi, V., Edwards, B., and Fäh, D. (2012). Characterizing the Vertical-to-Horizontal ratio of ground motion at soft-sediment sites. *Bull. Seismol. Soc. Am.*, 102(6):2741–2756.

Poggi, V. and Fäh, D. (2010). Estimating Rayleigh wave particle motion from three-component array analysis of ambient vibrations. *Geophys. J. Int.*, 180:251–267.